

Electron–Ion Coupling Breaks Energy Symmetry in Organic Electrochemical Transistors

Lukas M. Bongartz^{1,2*}, Garrett LeCroy¹, Tyler J. Quill¹, Nicholas Siemons¹, Gerwin Dijk¹, Adam Marks¹, Christina Cheng¹, Hans Kleemann², Karl Leo², Alberto Salleo¹

¹Department of Materials Science and Engineering, Stanford University, Stanford, CA 94305, USA

²Institute for Applied Physics, Technische Universität Dresden, Nöthnitzer Str. 61, 01187 Dresden, Germany

Abstract. Organic electrochemical transistors are extensively studied for applications ranging from bioelectronics to analog and neuromorphic computing. Despite significant advances, the fundamental interactions between the polymer semiconductor channel and the electrolyte, which critically determine the device performance, remain underexplored. Here, we examine the coupling between the benchmark semiconductor PEDOT:PSS and ionic liquids to explain the bistable and non-volatile behavior observed in OECTs. Using X-ray scattering and spectroscopy techniques, we demonstrate how the electrolyte modifies the channel composition, enhances molecular order, and reshapes the electronic and energetic landscape. Notably, the observed bistability arises from asymmetric and path-dependent energetics during doping and dedoping, resulting in two distinct, stable states, driven by a direct interaction between the electronic and ionic charge carriers. These findings highlight a compelling method to control charge carrier dynamics via the electrolyte, positioning it as a powerful yet underutilized tool for enabling novel device functionalities.

Introduction

Organic electrochemical transistors (OECTs) are a core technology for next-generation microscale devices that couple ionic and electronic charge carriers^{1,2}. With functional similarities to biological neurons, OECTs hold promise for applications such as bioelectronics^{3–6}, scalable neuromorphic computing^{7–9}, and analog spiking neurons^{10–12}. Essential to OECTs is the channel material where charge coupling occurs inside organic mixed ionic–electronic conductors (OMIECs)¹³ and modulation of the ion density induces changes in the electronic charge carrier concentration. The ionic–electronic coupling is harnessed when an OMIEC acts as the channel material between source and drain contacts, coupling to the gate through an electrolyte (Fig. 1a). A drain-source voltage V_{DS} drives electronic transport along the molecules’ π -systems, while a gate-source voltage V_{GS} regulates ion transport between the electrolyte and channel. In

maintaining charge neutrality, ions induce or compensate molecular charges, enabling dynamic de-/doping and control of the bulk conductivity.

Although a variety of systems have been explored as OECT channel materials^{13,14}, the most commonly deployed OMIEC is the polymer blend poly(3,4-ethylenedioxythiophene) polystyrene sulfonate (PEDOT:PSS, Fig.S1). Within this blend, PEDOT provides the π -backbone for electronic transport and is (p-)doped by the ionically conducting PSS. On the nano- and mesoscale, PEDOT:PSS forms cores, or “pancakes”^{15,16}, embedded in a PSS-rich matrix¹⁷⁻¹⁹, coexisting in regions of paracrystalline order and amorphous disorder (Fig. 1b). When operating PEDOT:PSS, semicrystalline regions charge first during doping, but efficient transport also requires the charging of amorphous regions to bridge the transport edge²⁰ in the heterogeneous energy landscape²¹. Due to its intrinsic doping, PEDOT:PSS-based OECTs generally work in depletion mode, switching from conductive to insulating with a positive gate voltage, typically achieved using water-based electrolytes like aqueous NaCl (Fig. 1c).

Extensive research has focused on fine-tuning the properties of PEDOT:PSS to suit various applications. For example, post-treatment with sulfuric acid (H_2SO_4) improves the long-term stability by enhancing crystallinity and removing excess PSS^{22,23}. Moreover, PEDOT:PSS-based OECTs can be operated in enhancement mode by utilizing molecular dedoping to reduce off-current and threshold voltage²⁴. Alternatively, different additives have been explored to induce non-volatility in neuromorphic computing, manifesting in a markedly hysteretic switching performance^{25,26}. Despite being effective, these approaches rely on additional processes and focus on modifying the semiconductor material. In that context, ionic liquids have gained increasing attention as water-free substitutes for the electrolyte, holding promise to improve the device performance in terms of temperature resilience and operation bandwidth^{27,28}. The most commonly deployed member of this class is 1-ethyl-3-methylimidazolium bis(trifluoromethylsulfonyl)imide ([EMIM][TFSI]), whose transfer curve is shown in Fig. 1d.

We recently demonstrated that the ionic liquid 1-ethyl-3-methylimidazolium ethyl sulfate ([EMIM][EtSO₄]) induces strongly non-volatile behavior in PEDOT:PSS-based OECTs without modifying the polymer semiconductor²⁹. The hysteretic behavior has previously been described by a thermodynamic framework, where bistable device operation arises from the balance of entropic and enthalpic contributions involved in the doping cycle³⁰. While this reasoning provides a macroscopic description of the system, a microscopic understanding of this phenomena is missing. Here, we investigate the coupling of PEDOT:PSS and ionic liquids using techniques such as X-ray photoelectron spectroscopy (XPS), grazing incidence wide-angle X-ray scattering (GIWAXS), Raman spectroscopy, and in-operando spectroelectrochemistry. Fitting the spectroscopic data to a vibronic model provides key insights into the energy landscape, uncovering a pronounced asymmetry in the de-/doping energetics. This asymmetry arises from a direct coupling between electronic and ionic charge carriers, a behavior absent in all of the studied reference systems, highlighting the choice of electrolyte as an effective

approach to tune the properties of electrochemical devices.

Main

Device Performance

A comparison of the OECT performance using aqueous NaCl solution (100 mM), [EMIM][TFSI], and [EMIM][EtSO₄] highlights the importance of the electrolyte (Fig. 1c–e). Besides a reduced threshold voltage, the [EMIM][EtSO₄] system stands out for two defining features. First, the device exhibits an exceptionally low off-current in the range of nA. Second, it is characterized by a strong hysteresis, which is also observed for [EMIM][TFSI] at a higher off-current level, but scarcely for NaCl. Notably, when an OECT is temporarily exposed to [EMIM][EtSO₄] but operated in NaCl, changes to threshold voltage and off-current persist, reminiscent of sustained molecular dedoping (Fig. S2). No hysteresis is observed when exchanging PEDOT:PSS for another OMIEC (Fig. S3). Since both ionic liquids contain the [EMIM]⁺ cation, the difference in device performance must relate to the different anion.

The origins of the transfer curve hysteresis in OECTs can be deconstructed from the fundamental relation for the electrical conductivity of the channel, which determines the drain current I_D :

$$\sigma(V_{GS}) = n(V_{GS}) \cdot \mu(V_{GS}) \cdot e, \quad (1)$$

where $n(V_{GS})$ is the charge carrier density, $\mu(V_{GS})$ is the hole mobility, and e is the elementary charge. The asymmetry between the doping and dedoping path thus arises from a path dependence of $n(V_{GS})$, $\mu(V_{GS})$, or both. Electronic mobility can exhibit path dependence due to charge-induced structural rearrangements and charge–charge interactions^{31,32}. However, we find identical hole mobilities in PEDOT:PSS OECTs with the [EMIM][EtSO₄] electrolyte in both the doped and undoped states (Supplementary Note 1): $\mu_d = (12.2 \pm 0.6) \text{ cm}^2 \text{ V}^{-1} \text{ s}^{-1}$ and $\mu_u = (11.6 \pm 0.6) \text{ cm}^2 \text{ V}^{-1} \text{ s}^{-1}$, indicating that the hysteresis primarily arises from the charge carrier density $n(V_{GS})$.

In a conventional transfer curve, where the gate voltage controls the drain current, the charge carrier density for a given gate voltage depends on the doping history. Similarly, the gate voltage required for a fixed charge carrier number differs depending on whether the system begins in the doped or undoped state. These quantities are linked via the (electro-)chemical potential, indicating that the same charge carrier density exhibits different energy levels when approached from either state. This is validated by means of an “inverted” transfer curve, where the number of charge carriers is controlled by a gate current I_G , and the corresponding gate-source voltage is measured. Fig. 1f shows the modulation in drain current upon applying 1 nA to the gate, followed by -1 nA (70s each). Effective de-/doping is observed, with the drain current varying over four orders of magnitude and saturating in on- and off-state. Fig. 1g overlays the two sweeps, confirming the absence of hysteresis as the charge carrier number is fixed. Instead, hysteresis appears as an 86 mV offset in the

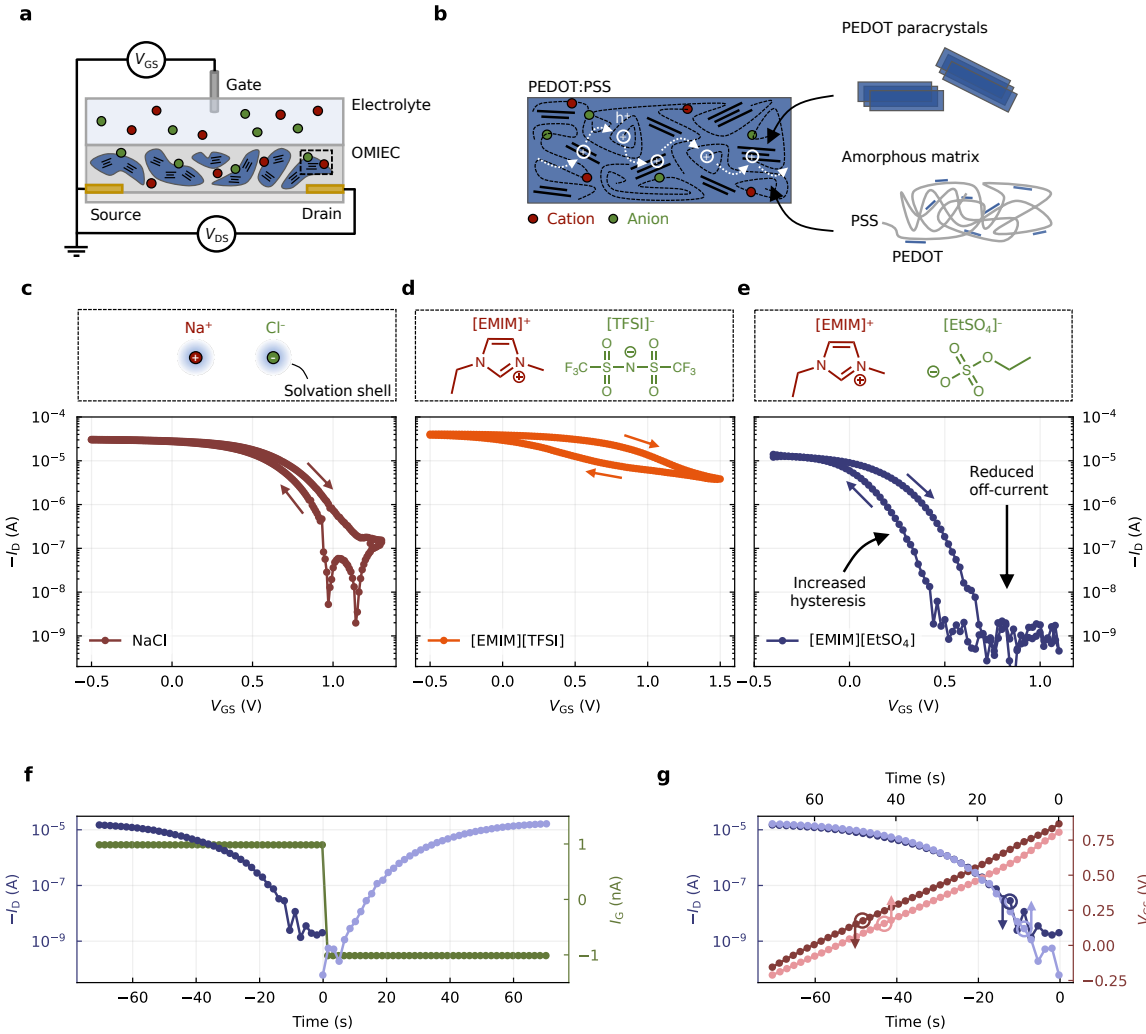


Fig. 1: OECTs with PEDOT:PSS channel and [EMIM][EtSO₄] electrolyte. (a) Generalized layout of an OECT with PEDOT:PSS channel. Devices in this worked typically featured a capacitive side-gate. (b) PEDOT:PSS is a heterogeneous material, where the electronic charge transport through paracrystalline entities is bridged by amorphous regions. (c–e) Transfer curves of OECTs with PEDOT:PSS channel and 100 mM aqueous NaCl, [EMIM][TFSI], and [EMIM][EtSO₄] electrolyte ($V_{DS} = -10$ mV). The hysteresis remains pronounced even for greatly reduced scan rates (Fig. S3). Devices featured the same geometry. (f) Operating an OECT (PEDOT:PSS with [EMIM][EtSO₄]) with a gate current instead of voltage ($V_{DS} = -10$ mV). (g) The folded I_D -response shows no hysteresis. Instead, the hysteresis reflects in the induced voltage between source and gate.

gate voltage V_{GS} . This confirms that fixing the number of charge carriers shifts the hysteresis to the gate voltage and suggests that dedoping is energetically less favorable than doping, consistent with the “clockwise” hysteresis loop in Fig. 1e. Probing the gate potential against a quasi-reference electrode confirms symmetric shifts with V_{GS} (Fig. S4), demonstrating that the hysteresis originates from shifts in chemical potential rather than external potential. Depending on the doping direction, charge carriers exhibit different energetics, suggesting changes in the energy landscape and density of states, which motivates further analysis of the interactions between the electrolyte and

semiconductor.

Semiconductor Analysis

The composition and morphology of the polymer-electrolyte system was studied through XPS, X-ray scattering, and Raman spectroscopy. XPS analysis of PEDOT:PSS thin films exposed to [EMIM][TFSI] and [EMIM][EtSO₄] reveals several changes introduced by the ionic liquids. Both treatments reduce the sodium signal, attributed to residual ions bound as Na:PSS^{33,34}, with [EMIM][EtSO₄] erasing it completely (Fig. 2a). The N 1s spectra show an increased signal from [EMIM]⁺ (Fig. 2b), indicating ion exchange in both cases. The C 1s data (Fig. S5a), lacking a CF₃ signal that would originate from the nitrogen-containing [TFSI]⁻ anion, supports this conclusion for both ionic liquids, albeit to different extents. The O 1s core level region further highlights a PSS removal, which is much more pronounced for [EMIM][EtSO₄] (Fig. 2c). This electrolyte also shows a distinctive shoulder at ~ 531 eV, attributed to the [EtSO₄]⁻ anion^{35,36}, suggesting that [EMIM]⁺ is partially balanced by its native anion. With [EMIM][TFSI], in contrast, [EMIM]⁺ is retained independently. To quantify these changes, O 1s and S 2p core level data (Fig. S5b) are fitted with Gaussian-Lorentzian functions, revealing a change in PEDOT-to-PSS ratio from 1:3.39 to 1:3.10 with [EMIM][TFSI], and a much larger reduction to 1:1.61 with [EMIM][EtSO₄]. Based on these ratios, the ion exchange ratio between PEDOT:PSS and [EMIM][EtSO₄] is estimated at approximately

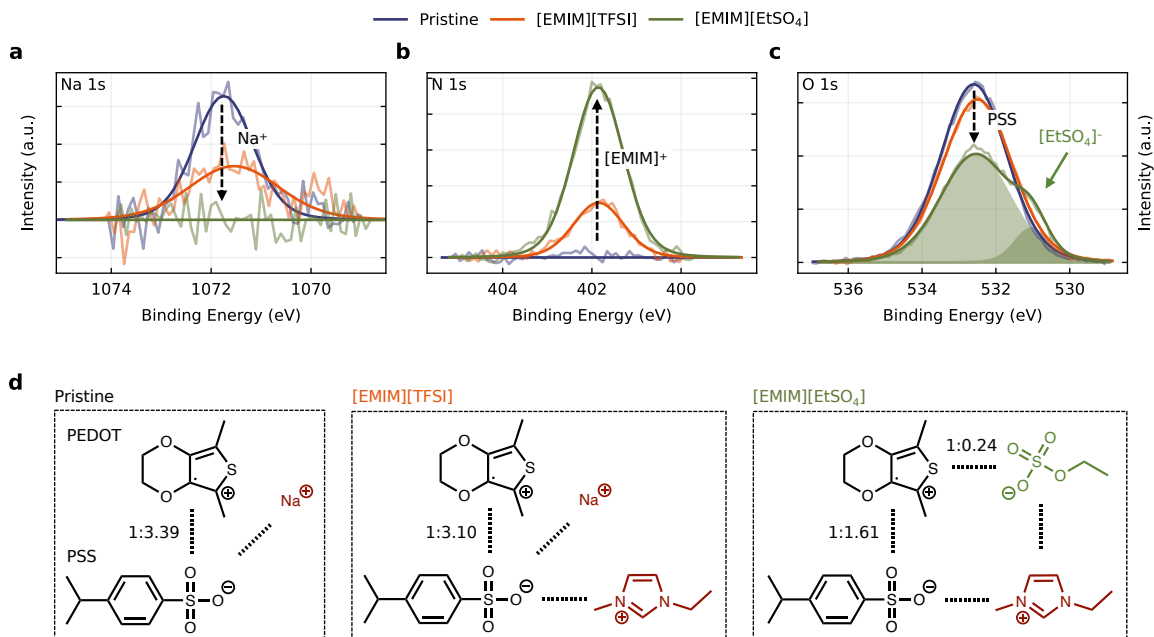


Fig. 2: XPS thin-film analysis. (a–c) XPS spectra (raw and fit) of pristine and electrolyte-treated PEDOT:PSS thin films with core levels (a) Na 1s, (b) N 1s, and (c) O 1s. See Fig. S5 for C 1s and S 2p spectra. (d) Illustration of the material composition of pristine PEDOT:PSS and after exposure to the ionic liquids [EMIM][TFSI] and [EMIM][EtSO₄]. With the latter, PEDOT:PSS transitions to a composite that intrinsically retains both the cat- and anion of the electrolyte.

24% (Supplementary Note 2). These findings reveal that [EMIM][TFSI] induces partial cation exchange, replacing PSS-bound Na^+ with $[\text{EMIM}]^+$ while leaving the PEDOT:PSS ratio largely unchanged. In contrast, [EMIM][EtSO₄] drives complete cation exchange, accompanied by significant PSS removal and retention of $[\text{EtSO}_4]^-$, leading us to conclude the formation of a quaternary ionic system, consistent with previous reports (Fig. 2d)³⁷.

We attribute this interplay between PEDOT:PSS and [EMIM][EtSO₄] to two main factors. First, [EMIM][EtSO₄] stands out by a markedly high dielectric constant ($\epsilon_{[\text{EMIM}][\text{EtSO}_4]} = 27.9$ vs. $\epsilon_{[\text{EMIM}][\text{TFSI}]} = 12.3$)^{38,39}, enabling it to penetrate the thin-film and shield the interactions between PEDOT and PSS, allowing the polymers to separate^{40,41}. Second, the chemical similarity between $[\text{EtSO}_4]^-$ and PSS (Fig. 2d), both containing SO₃-groups, suggests comparable binding energetics towards PEDOT and $[\text{EMIM}]^+$. In fact, DFT studies by de Izarra et al. estimate the free energy of ion exchange between PEDOT:PSS and [EMIM][EtSO₄] as < 20 meV⁴⁰, suggesting a thermally activated exchange ratio of $\sim 32\%$, similar to our XPS results (Supplementary Note 3).

Furthermore, we infer that the reduction in off-current as observed in the OECT (Fig. 1e) can be explained by the lower PSS content through two mechanisms. First, interlocked PSS can act as a parasitic dopant, introducing surplus charge carriers and contributing to leakage conductivity in the off-state ($n(V_{\text{GS}})$ in Eq. 1). Second, PSS supports the bulk conductivity in PEDOT:PSS by facilitating electronic tunneling¹⁹ ($\mu(V_{\text{GS}})$ in Eq. 1). Finally, the high polarity of [EMIM][EtSO₄] enhances the film penetration and polymer access for dedoping, which does not apply to the less polar [EMIM][TFSI].

The two-dimensional diffraction patterns for pristine and [EMIM][EtSO₄]-treated thin films are shown in Fig. 3a (see Fig. S6 for all electrolytes), with normalized GIWAXS profiles in Fig. 3b. For the pristine film, key features include (100) and (200) lamellar reflections at $q_z \sim 0.35 \text{ \AA}^{-1}$ and $q_z \sim 0.7 \text{ \AA}^{-1}$ ($d_{100} = 1.80 \text{ nm}$), an isotropic PSS halo at $q_z \sim 1.38 \text{ \AA}^{-1}$, and a PEDOT π -stacking peak at $q_z = 1.85 \text{ \AA}^{-1}$ ($d_{010} = 0.34 \text{ nm}$)^{22,37,42}. Exposure to [EMIM][EtSO₄] induces several changes. The PSS halo broadens and shifts to $q_z = 1.44 \text{ \AA}^{-1}$, reflecting PSS removal and overlapping reflections from [EMIM][EtSO₄]⁴³. The PEDOT π -stacking peak increases in intensity, indicating enhanced crystallinity, which aligns with previous studies³⁷ and resembles structures observed with PEDOT:PSS films post-treated with sulfuric acid^{22,23}. A new shoulder emerges at $q_z = 0.50 \text{ \AA}^{-1}$ ($d = 1.26 \text{ nm}$), attributed to the lamellar structure of retained ionic liquid⁴³, while the lamellar reflections decrease in relative intensity. For the reference systems, NaCl introduces minimal changes, with a more intense low-angle region and a minor decrease in π -stacking distance. [EMIM][TFSI] induces similar but less pronounced effects compared to [EMIM][EtSO₄], lacking the shoulder at $q_z \sim 0.50 \text{ \AA}^{-1}$ and showing weaker changes to the PSS halo.

A closer examination of the molecular interactions is pursued through vibrational and optical spectroscopy. Thin-film UV-Vis and IR spectroscopy reveal no significant

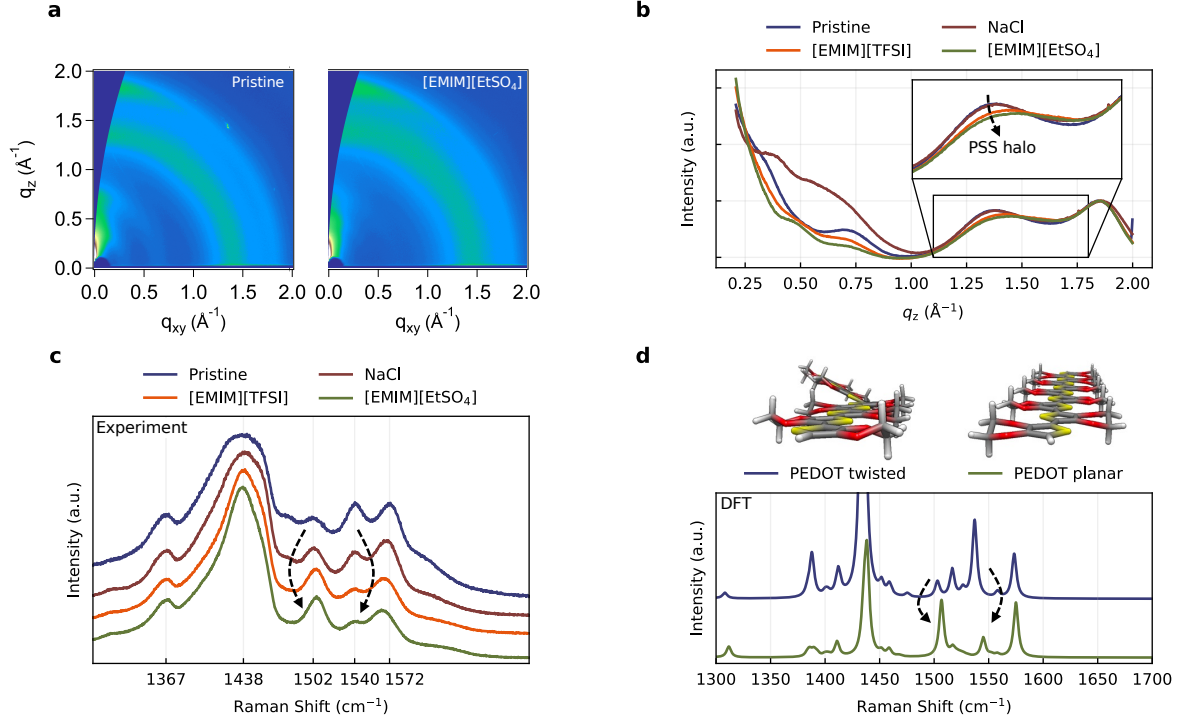


Fig. 3: Semiconductor morphology. (a) 2D GIWAXS pattern of pristine and [EMIM][EtSO₄]-treated PEDOT:PSS. (b) Vertical GIWAXS profiles with high-angle magnification in the inset. All spectra are normalized with respect to their (010) signal. (c) Raman spectra (high-energy range) recorded with $\lambda_{\text{exc}} = 532 \text{ nm}$. The full spectra and peak assignment are provided in Fig. S9 and Tab. S2. (d) DFT calculations of distorted and planar PEDOT resemble the experimental observation in (c).

changes across the systems, except for the sample treated with [EMIM][EtSO₄], which exhibits a more pronounced polaron absorbance and a vibronic signature attributed to the retained [EMIM]⁺ cation (Fig. S7, S8). As a complementary technique, Raman spectroscopy provides insights into vibrational modes that are weak or inactive in IR. The low-energy region ($< 1300 \text{ cm}^{-1}$, Fig. S9) again shows no significant changes for any electrolyte, apart from a reduction in PSS in the system treated with [EMIM][EtSO₄]. The most intense bands are found above 1300 cm^{-1} , with the principal peak of PEDOT at 1438 cm^{-1} (Fig. 3c). No significant shift is observed after exposure to any electrolyte ($< 4 \text{ cm}^{-1}$). Instead, we find a gradual decrease in bandwidth, with [EMIM][EtSO₄] reducing the full width at half maximum from 106 cm^{-1} to 57 cm^{-1} (Fig. S10). Given that the peak bandwidth reflects the statistical distribution of conjugation lengths⁴⁴, we interpret this as evidence of [EMIM][EtSO₄] arranging and homogenizing PEDOT. The higher-sided signals in Fig. 3c, assigned to asymmetric mid- and end-chain modes, exhibit a peculiar intensity shift. The 1572 cm^{-1} signal remains largely unchanged, while the 1502 cm^{-1} mode increases and the 1540 cm^{-1} mode nearly vanishes with [EMIM][EtSO₄], mirroring the pattern reported for H₂SO₄ treatment⁴⁵, which affirms the planarization of PEDOT. To support this interpretation, we perform DFT calculations of the Raman signals with PEDOT in distorted and planar configuration (Supple-

mentary Note 4). As shown in Fig. 3d, the calculations agree with the experimental data, demonstrating that the transition from a distorted to a planar configuration drives the change in relative intensities and confirming the homogenizing effect of [EMIM][EtSO₄] on PEDOT.

These studies demonstrate the salient impact of the ionic liquid [EMIM][EtSO₄] on PEDOT:PSS. On the device level, this manifests in an enhanced OECT performance, including a reduction in threshold voltage and off-current. On the molecular level, this is paralleled by an enhanced crystallization of PEDOT and the removal of PSS. We propose that these changes also relate to the asymmetric doping behavior in OECTs, which we examine spectroscopically.

In-Operando Doping Studies

Charging the polymer to different doping degrees via chronoamperometry, simultaneously measuring its spectral features provides insights into the morphological environments and energetics involved. Fig. 4a and b show the discharging cycle of PEDOT:PSS with [EMIM][EtSO₄] and [EMIM][TFSI] electrolyte (see Fig. S11 and S12 for both cycles).

The ionic liquid [EMIM][EtSO₄] causes a feature-rich absorbance signature of PEDOT:PSS, resembling the NaCl reference sample (Fig. S13) more closely than [EMIM][TFSI]. The dedoped states under [EMIM][EtSO₄] (blue) show stronger suppression below 1.6 eV, attributed to polaronic excitation, which directly correlates with the reduced OECT off-current (Fig. 1e). Absorbance above 1.6 eV originates from excitonic transitions involving states of coupled electronic and vibrational coordinates (Fig. S14), where amorphous regions broaden the density of states, while aggregates narrow it^{46,47}. Accordingly, the absorbance spectra of PEDOT:PSS with [EMIM][TFSI] indicates a considerably more amorphous PEDOT morphology. Furthermore, the increased intensity of the 0–0 transition relative to the 0–1 transition for [EMIM][EtSO₄] (Fig. 4c) highlights dominant intrachain coupling. This contrasts with the NaCl sample (Fig. S13), where more balanced intensities suggest a mix of intra- and interchain coupling^{47,48}. This observation resonates strongly with the crystallizing and ordering impact of [EMIM][EtSO₄] on PEDOT found earlier.

We expand on these findings using the model developed by Spano⁴⁸ to fit the absorbance features to the underlying vibronic transition probabilities (Supplementary Note 5). This analysis provides the absorbance of aggregated PEDOT, where the integrated absorbance indicates their relative contribution to the total absorbance (Fig. 4c). The residual absorbance above ~ 1.6 eV is assigned to amorphous PEDOT. Tracking the aggregate fraction (AF) throughout the doping cycle, excluding the polaronic regime, reveals a clear hysteresis for the sample treated with [EMIM][EtSO₄] (Fig. 4d). The aggregate fraction represents the fraction of PEDOT aggregates relative to the total PEDOT (aggregates and amorphous) at a given potential. Its decrease

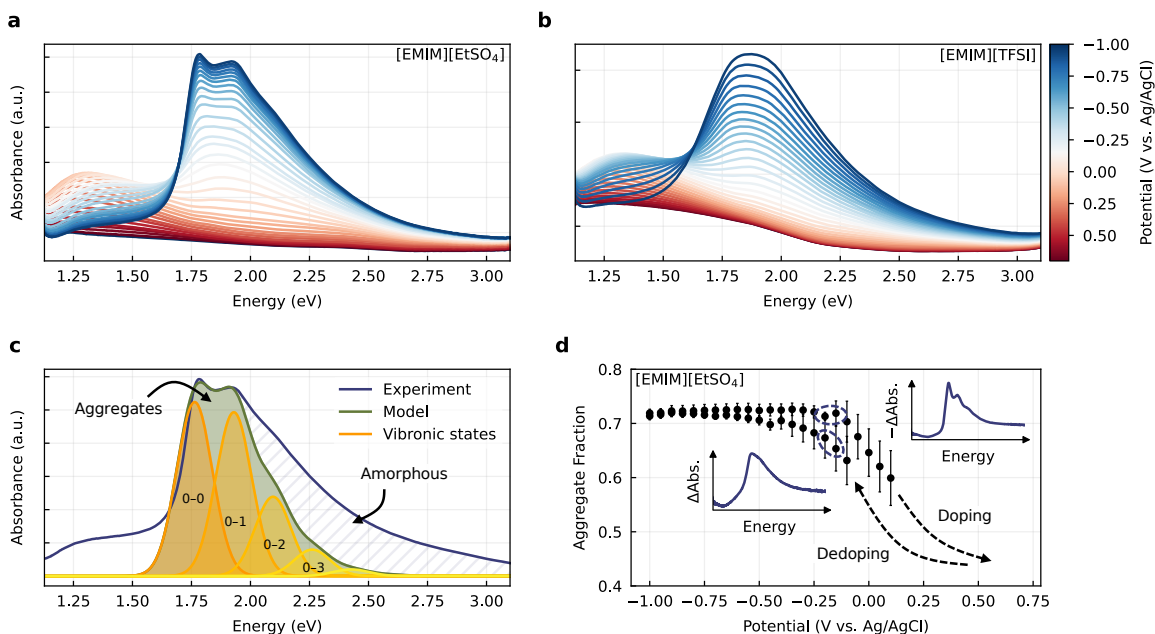


Fig. 4: In-operando doping studies. (a, b) Absorbance spectra (discharging cycle) of PEDOT:PSS with [EMIM][EtSO₄] and [EMIM][TFSI] electrolyte. [EMIM][EtSO₄] produces feature-rich spectra, reflecting high aggregation, while [EMIM][TFSI] suggests an amorphous nature. (c) Absorbance spectra are fitted using a vibronic model that incorporates the lowest five vibronic transitions (0–0 through 0–4). This approach allows to infer the absorbance share owing to undoped PEDOT in aggregates and amorphous regions. (d) From this, the aggregate fraction (AF) follows for each potential. The omitted potential regime cannot be reliably fitted due to dominant polaron absorbance (Supplementary Note 5). Insets: Differential absorbance for the dis-/charging step between potentials of -0.2 V and -0.15 V, revealing a stark asymmetry in their spectral signatures.

during doping shows that aggregates charge first, consistent with their oxidation potential being closer to the midgap compared to amorphous regions^{21,49}. During dedoping, on the other hand, these aggregates release their charge the latest and in fact, only at an increased potential compared to their charging, giving rise to the hysteresis.

We underpin this analysis by examining the differential spectra of consecutive dis-/charging steps (Fig. 4d, insets). Representing the absorbance lost during doping or gained during dedoping, differentials indicate the domains where charges are injected or extracted. At the start of doping, highly feature-rich spectra confirm prioritized charging of aggregates, followed by amorphous regions as the spectra blur out. During dedoping, this sequence is reversed but occurs with an offset in potential. The insets of Fig. 4d both correspond to the -0.2 V to -0.15 V potential step, highlighting that, at this potential increment, doping predominantly charges ordered regions, whereas dedoping mainly affects amorphous regions. The discharging of aggregates only begins at potentials below -0.35 V (Fig. S15). This observation directly links to the findings from Fig. 1g: a higher potential is required to extract charges than to inject them.

This energetic asymmetry is also evident in the charge carrier density (n) in Fig. 5a (see also Fig. S15). Charge injection begins at -0.3 V, with a steeper slope than charge

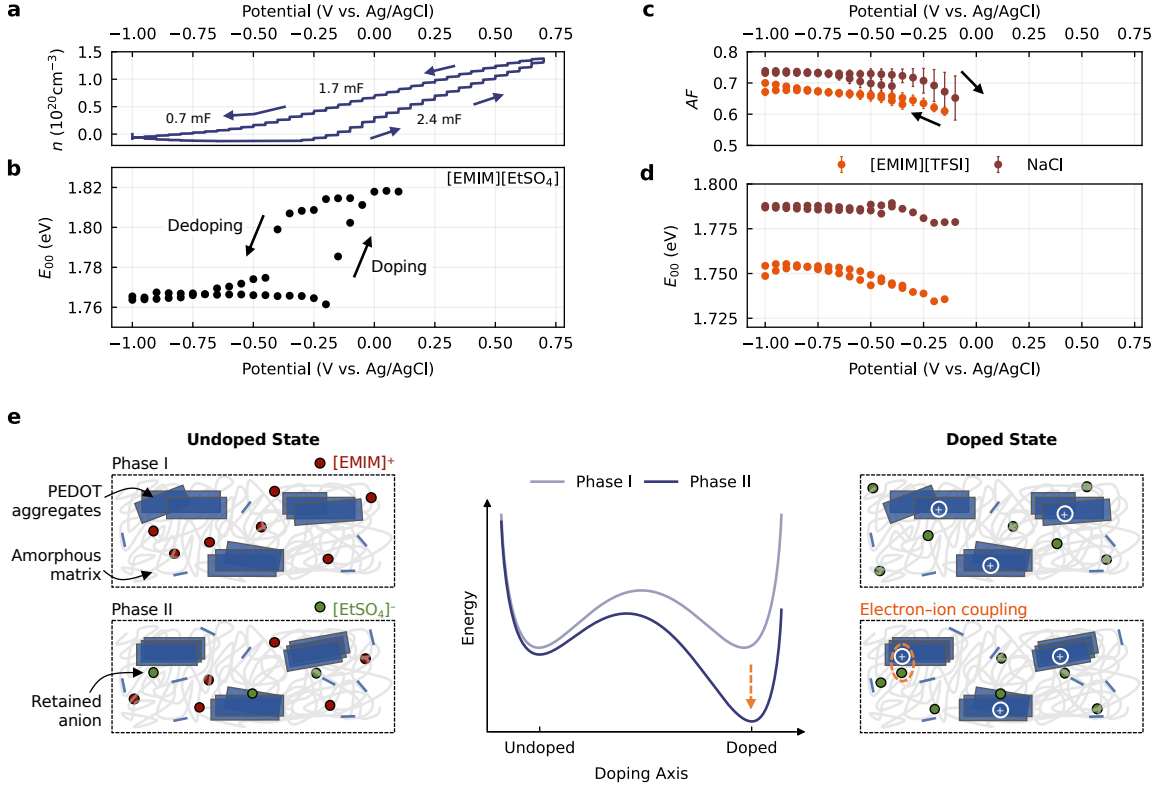


Fig. 5: Energetics of the doping cycle. (a) Charge carrier density n as a function of applied potential. See also Fig. S15. (b) E_{00} energies extracted from absorbance fits (Fig. 4c), showing a marked asymmetry between doping and dedoping. (c, d) Aggregate fraction (AF) and E_{00} energies for samples of $[EMIM][TFSI]$ and $NaCl$ electrolyte. (e) The doping cycle of PEDOT:PSS with $[EMIM][EtSO_4]$ affects the biphasic aggregate distribution of entities with and without the $[EtSO_4]^-$ anion (Phases I and II). In the doped state, $[EtSO_4]^-$ stabilizes the polaron, creating a bimodal binding pattern and asymmetric energetics for doping and dedoping.

extraction in the same regime (2.4 mF vs. 1.7 mF). Notably, discharging kinks further at around -0.5 V (0.7 mF), suggesting a bimodal stabilization of charge carriers.

The relative stability of the species involved in the doping cycle can be inferred from their electronic transition energies, where more ordered structures exhibit lower values (red-shift) due to enhanced coherence and stabilization. We use the E_{00} quantity, representing the purely electronic transition between fundamental phonon modes, as extracted from the optical absorbance fits (Fig. 5b). This analysis reveals an asymmetry closely aligned with the charging steps in Fig. 5a. As doping progresses, E_{00} rises stepwise from 1.765 eV to 1.818 eV, marking a shift of 53 meV, where it stabilizes. This rise reverses during dedoping, reflecting the bimodal stabilization with a leveling slope at around -0.45 V. Meanwhile, dedoping is offset by approximately 0.3 V in potential, indicating an energetic stabilization of the doped state. Given the 53 meV energy difference, the entities underlying Fig. 5b cannot solely represent aggregated and amorphous regions, as these typically exhibit energy gaps in the hundreds of meV⁵⁰. Instead, they correspond to different aggregate types with varying degrees of order, consistent with Fig. 4d, where a high aggregate fraction persists even at potentials of

raised E_{00} energies.

Fig. 5c and d show the aggregate fraction and E_{00} energies for samples with [EMIM][TFSI] and NaCl electrolyte, where none of the discussed effects are observed. Instead, we note a minimal decrease in E_{00} during doping without any potential shift. This aligns with our XPS studies, as [EMIM][EtSO₄] uniquely retains its anion due to aligned binding energetics and low ion exchange barriers, forming the quaternary ionic system of Fig. 2d. Hence, the two aggregate types appear as entities with and without [EtSO₄]⁻, with increased molecular order and stabilization expected for PEDOT accompanied by [EtSO₄]⁻.

In this biphasic picture, [EtSO₄]⁻ is understood to stabilize polarons created during doping (Fig. 5e). Its small molecular volume enables it to access PEDOT aggregates inaccessible to PSS, providing an energetic lowering of doped entities and creating an energetic asymmetry between doping and dedoping. This process may also involve subtle molecular rearrangements of [EtSO₄]⁻, potentially orienting toward charged PEDOT aggregates. Tentative evidence for such rearrangements may be found in the differential absorbance spectra, which exhibit a clear asymmetry in the 0-0/0-1 transition ratio between doping and dedoping, indicative of a disruption in the local electronic environment (Fig. S15). However, further verification of this hypothesis is challenging, as in-operando imaging techniques remain less accessible for PEDOT:PSS compared to systems with stronger diffraction³¹.

Conclusion

In this study, we investigated the unique performance of the OECT system composed of PEDOT:PSS and the ionic liquid [EMIM][EtSO₄]. This combination has previously been shown to exhibit exceptional device characteristics, including a significantly suppressed off-current and pronounced non-volatile, hysteretic behavior³⁰. We find that [EMIM][EtSO₄] induces multiple beneficial effects in PEDOT:PSS, including the formation of a quaternary ionic system and enhanced molecular order facilitated by the [EtSO₄]⁻ anion. Its electronic properties and small size enable [EtSO₄]⁻ to stabilize polarons in its vicinity, lowering the energy of the doped state and creating an energetic asymmetry between doping and dedoping. While doping is energetically favored, dedoping requires overcoming this stabilization, resulting in distinct switching energetics.

These results underscore the critical interplay between the components of electrochemical devices, particularly the direct interaction between the electronic charges in the OMIEC and the ionic charges supplied by the electrolyte. This coupling is especially pronounced in polar ionic liquids, whose molecular ions match the electronic structure of the charged OMIEC in terms of dipole moment and polarizability, promoting a direct coupling of their electron densities. Conventional electrolytes like aqueous NaCl hinder such coupling due to their electronically isotropic, atomic ions and interfering solvation shells. While much attention has been devoted to the optimization of OMIECs,

the design space of electrolytes, in particular molecular systems, remains largely unexplored. As this study shows, it holds great promise to impose novel functionalities into electrochemical systems that are inaccessible with conventional electronic materials. Unlocking these dynamics offers opportunities to, among others, advance post-binary computing, enabling systems founded on complex behaviors and multi-state stability⁵¹.

Methods

Device fabrication. Microfabrication of OECTs was performed on silicon wafer substrates with a 1 μm thermal oxide employing previous established protocols that involve a lift-off process to pattern the source and drain contacts and an additional dry lift-off with a sacrificial Parylene C layer to pattern PEDOT:PSS⁵². The metal interconnects were patterned with photolithography using a LOL2000/SPR3612 bilayer resist and a maskless aligner (Heidelberg MLA150) followed by the deposition of 5/100 nm Ti/Au (AJA e-beam evaporator) and lift-off. Patterning of the Parylene C encapsulation and PEDOT:PSS (channel and gate) were performed in a combined process through a dry lift-off process using a sacrificial Parylene C layer. First, 2 μm Parylene C was deposited using 3-(trimethoxysilyl)propyl methacrylate as an adhesion promotor (Special Coating Systems PDS 2010 Labcoter). After the deposition of a diluted Micro-90 anti-adhesion layer, a second layer of 2 μm Parylene C was deposited. Channel and gate were defined by etching the two layers of Parylene C (Plasma-Therm oxide etcher) using a 75 nm Ti etch mask that was patterned using SPR 3612 photoresist and a metal etcher (Plasma-Therm metal etcher). PEDOT:PSS was deposited by preparing a solution of Hereaus Clevis PH 1000, 6 vol% ethylene glycol (EG), 1 vol% (3-glycidyloxypropyl)trimethoxysilane (GOPS), and 0.1 vol% dodecyl benzene sulfonic acid (DBSA), all of which were obtained from Sigma Aldrich. The solution was spun at 1000 rpm for 2 min and baked at 120 °C for 5 min. The sacrificial Parylene C layer was peeled off followed by an additional baking of 15 min. Dies were rinsed in deionized water and dried for another 5 min at 120 °C. Devices used in this work had dimensions of $W = 100 \mu\text{m}$, $L = 100 \mu\text{m}$, and a channel thickness of 100 nm. The gate area was $3.8 \times 2.2 \text{ mm}$.

Electrical characterization. Electrical transistor characterizations were performed using a Keithley 2612 SourceMeter with custom LabVIEW and SweepMe! (sweep-me.net) software. Referenced measurements were carried out by simultaneously employing a BioLogic SP-300 potentiostat with an Ag quasi-reference electrode.

XPS measurements. PEDOT:PSS thin-films of same size were exposed to the ionic liquids [EMIM][EtSO₄] and [EMIM][TFSI] for 5 min and the excess electrolyte was removed by rinsing with deionized water. X-ray photoelectron spectroscopy (XPS) was performed using a PHI VersaProbe 4 with a monochromatized Al K α source (1486.6 eV, 50 W, 200 μm spot size) and a pass energy of 55 eV. An electron flood gun and low-energy Ar⁺ ions were used to neutralize the sample and prevent substrate charging. Binding energies were corrected to the C–C peak in the C 1s signal at 284.8 eV. For all

collections, the angle between the sample surface and the detector was 45° . To ensure that the compositions of the measured spectra were representative of the bulk, samples were sputtered with a gas cluster ion beam source (Ar_{2000}^+ , 10 kV) for 1 min prior to all collections. The spectra were smoothed using the five-point quadratic Savitzky-Golay method and then fit to Gaussian-Lorentzian lineshapes and a Shirley-type background in CasaXPS software.

GIWAXS measurements. Grazing incidence wide-angle X-ray scattering (GIWAXS) measurements were carried out at the Stanford Synchrotron Radiation Lightsource (SSRL) on beam line 11-3 using a CCD area detector (Rayonix MAR 225) at a distance of 319.998 mm and an incidence angle of 0.1° . The incident energy was 12.73 keV. The beam path was flooded with helium to prevent air scattering. Data was corrected for geometric distortion arising from the flat detector architecture and normalized by exposure time and monitor counts. Analysis was performed using Nika 1D SAXS⁵³ and WAXS tools⁵⁴ software in Igor Pro. The reported quantities q_{xy} and q_z refer to the in-plane and out-of-plane scattering vector relative to the substrate. q_z lineouts were taken from χ -slices from -20° to 20° with respect to the q_z direction. Samples featured similar sizes, allowing for a semi-quantitative comparison of intensities.

DFT calculations. Density functional theory (DFT) calculations for the Raman experiment were carried out using the Gaussian16 software package⁵⁵ with a B3LYP⁵⁶⁻⁵⁸ functional and 6-311G basis set. The incident laser energy was matched to the experiment (2.329 eV). Details are provided in Supplementary Note 4.

UV-Vis-IR spectroscopy. Solid-state UV-Vis-IR spectroscopy was performed using an Agilent Cary 6000i UV-Vis-NIR Spectrophotometer and a Nicolet iS50R Fourier Transform Infrared (FTIR) spectrometer. For sample preparation, PEDOT:PSS was spun onto CaF_2 -substrates (2000 rpm for 2 min) and immersed into the electrolyte for 5 min, followed by rinsing in deionized water.

Raman spectroscopy. Raman spectroscopy was performed using a Horiba Labram HR Evolution confocal Raman microscope with an Andor CCD detector. A continuous wave 532 nm excitation laser was used and Raman scatter was collected through an objective in backscattering geometry ($100\times$, 0.6 NA). The scattered light was passed through a long-pass filter ($\sim 100 \text{ cm}^{-1}$) and dispersed with an 1800 gr mm^{-1} grating.

Spectroelectrochemistry. Spectroelectrochemical measurements were carried out using a home-built spectrometer with an Ocean Optics light source (tungsten-halogen light source) and an Ocean Optics QEPro detector. A quartz cuvette (20 mm optical path length) was used to conduct measurements in transmission mode. For sample preparation, PEDOT:PSS was spun onto indium-tin-oxide-coated glass substrates (ITO), covering 2.7 cm^2 in a thickness of 380 nm, as verified by profilometry (Bruker Dektak XT profilometer). Samples were placed in the cuvette filled with electrolyte to form a 3-electrode cell with a Pt mesh counter electrode, an eDAQ leakless Ag/AgCl reference electrode, and the PEDOT:PSS-coated ITO substrate working electrode. The cuvette was capped and purged with Ar gas. The electrochemical potential was controlled using an Ivium CompactStat potentiostat (chronoamperometry). The

potential at the working electrode was modulated in increments of 50 mV between -1.0 V and 0.7 V, holding each potential for 30 s. Spectra were recorded every 100 ms with an integration time of 10 ms and averaged over the final 10 s at each potential step, to best represent the steady-state. Details on the vibronic fits are provided in Supplementary Note 5.

References

1. Friedlein, J. T., McLeod, R. R. & Rivnay, J. Device physics of organic electrochemical transistors. *Organic Electronics* **63**, 398–414 (2018).
2. Rivnay, J. *et al.* Organic electrochemical transistors. *Nature Reviews Materials* **3**, 1–14 (2018).
3. Cea, C. *et al.* Integrated internal ion-gated organic electrochemical transistors for stand-alone conformable bioelectronics. *Nature Materials* **22**, 1227–1235 (2023).
4. Rashid, R. B., Ji, X. & Rivnay, J. Organic electrochemical transistors in bioelectronic circuits. *Biosensors and Bioelectronics* **190**, 113461 (2021).
5. Nawaz, A., Liu, Q., Leong, W. L., Fairfull-Smith, K. E. & Sonar, P. Organic electrochemical transistors for in vivo bioelectronics. *Advanced Materials* **33**, 2101874 (2021).
6. van Doremaele, E., Ji, X., Rivnay, J. & van de Burgt, Y. A retrainable neuromorphic biosensor for on-chip learning and classification. *Nature Electronics* **6**, 765–770 (2023).
7. Fuller, E. J. *et al.* Parallel programming of an ionic floating-gate memory array for scalable neuromorphic computing. *Science* **364**, 570–574 (2019).
8. van De Burgt, Y., Melianas, A., Keene, S. T., Malliaras, G. & Salleo, A. Organic electronics for neuromorphic computing. *Nature Electronics* **1**, 386–397 (2018).
9. Huang, W. *et al.* Vertical organic electrochemical transistors for complementary circuits. *Nature* **613**, 496–502 (2023).
10. Sarkar, T. *et al.* An organic artificial spiking neuron for in situ neuromorphic sensing and biointerfacing. *Nature Electronics* **5**, 774–783 (2022).
11. Harikesh, P. C. *et al.* Ion-tunable antiambipolarity in mixed ion–electron conducting polymers enables biorealistic organic electrochemical neurons. *Nature Materials* **22**, 242–248 (2023).
12. Zhu, Y. *et al.* Leaky Integrate-and-Fire Neuron Based on Organic Electrochemical Transistor for Spiking Neural Networks with Temporal-Coding. *Advanced Electronic Materials*, 2300565 (2023).
13. Paulsen, B. D., Tybrandt, K., Stavrinidou, E. & Rivnay, J. Organic mixed ionic–electronic conductors. *Nature Materials* **19**, 13–26 (2020).
14. Tropp, J., Meli, D. & Rivnay, J. Organic mixed conductors for electrochemical transistors. *Matter* **6**, 3132–3164 (2023).
15. Kayser, L. V. & Lipomi, D. J. Stretchable conductive polymers and composites based on PEDOT and PEDOT:PSS. *Advanced Materials* **31**, 1806133 (2019).
16. Ahmad, Z., Azman, A. W., Buys, Y. F., Sarifuddin, N., *et al.* Mechanisms for doped PEDOT:PSS electrical conductivity improvement. *Materials Advances* **2**, 7118–7138 (2021).

17. Takano, T., Masunaga, H., Fujiwara, A., Okuzaki, H. & Sasaki, T. PEDOT nanocrystal in highly conductive PEDOT:PSS polymer films. *Macromolecules* **45**, 3859–3865 (2012).
18. Rivnay, J. *et al.* Structural control of mixed ionic and electronic transport in conducting polymers. *Nature Communications* **7**, 1–9 (2016).
19. Keene, S. T. *et al.* Efficient electronic tunneling governs transport in conducting polymer-insulator blends. *Journal of the American Chemical Society* **144**, 10368–10376 (2022).
20. Kang, S. D. & Snyder, G. J. Charge-transport model for conducting polymers. *Nature Materials* **16**, 252–257 (2017).
21. Keene, S. T. *et al.* Hole-limited electrochemical doping in conjugated polymers. *Nature Materials* **22**, 1121–1127 (2023).
22. Kim, S.-M. *et al.* Influence of PEDOT:PSS crystallinity and composition on electrochemical transistor performance and long-term stability. *Nature Communications* **9**, 1–9 (2018).
23. Kim, N. *et al.* Highly conductive PEDOT:PSS nanofibrils induced by solution-processed crystallization. *Advanced Materials* **26**, 2268–2272 (2014).
24. Keene, S. T. *et al.* Enhancement-mode PEDOT:PSS organic electrochemical transistors using molecular de-doping. *Advanced Materials* **32**, 2000270 (2020).
25. Van De Burgt, Y. *et al.* A non-volatile organic electrochemical device as a low-voltage artificial synapse for neuromorphic computing. *Nature Materials* **16**, 414–418 (2017).
26. Ji, X. *et al.* Mimicking associative learning using an ion-trapping non-volatile synaptic organic electrochemical transistor. *Nature Communications* **12**, 1–12 (2021).
27. Melianas, A. *et al.* Temperature-resilient solid-state organic artificial synapses for neuromorphic computing. *Science Advances* **6**, eabb2958 (2020).
28. Zhong, Y. *et al.* Ionic Liquid Gated Organic Electrochemical Transistors with Broadened Bandwidth. *ACS Applied Materials & Interfaces* **16**, 61457–61466 (2024).
29. Weissbach, A. *et al.* Photopatternable solid electrolyte for integrable organic electrochemical transistors: operation and hysteresis. *Journal of Materials Chemistry C* **10**, 2656–2662 (2022).
30. Bongartz, L. M. *et al.* Bistable organic electrochemical transistors: enthalpy vs. entropy. *Nature Communications* **15**, 6819 (2024).
31. Quill, T. J. *et al.* An ordered, self-assembled nanocomposite with efficient electronic and ionic transport. *Nature Materials* **22**, 362–368 (2023).
32. Quill, T. J. *et al.* Charge Carrier Induced Structural Ordering And Disorder in Organic Mixed Ionic Electronic Conductors. *Advanced Materials*, 2310157 (2024).
33. Cho, H., Cho, W., Kim, Y., Lee, J.-g. & Kim, J. H. Influence of residual sodium ions on the structure and properties of poly (3,4-ethylenedioxythiophene): poly(styrenesulfonate). *RSC Advances* **8**, 29044–29050 (2018).
34. Lyu, D. *et al.* Operando NMR electrochemical gating studies of ion dynamics in PEDOT:PSS. *Nature Materials* **22**, 746–753 (2023).
35. Gottfried, J. *et al.* Surface studies on the ionic liquid 1-ethyl-3-methylimidazolium ethylsulfate using X-ray photoelectron spectroscopy (XPS). *Zeitschrift für Physikalische Chemie* **220**, 1439–1453 (2006).
36. Jurado, L. A. *et al.* Effect of the environmental humidity on the bulk, interfacial and nanoconfined properties of an ionic liquid. *Physical Chemistry Chemical Physics* **18**, 22719–22730 (2016).

37. Kee, S. *et al.* Controlling molecular ordering in aqueous conducting polymers using ionic liquids. *Advanced Materials* **28**, 8625–8631 (2016).
38. Weingärtner, H. The static dielectric constant of ionic liquids. *Zeitschrift für Physikalische Chemie* **220**, 1395–1405 (2006).
39. Singh, T. & Kumar, A. Static dielectric constant of room temperature ionic liquids: internal pressure and cohesive energy density approach. *The Journal of Physical Chemistry B* **112**, 12968–12972 (2008).
40. De Izarra, A., Park, S., Lee, J., Lansac, Y. & Jang, Y. H. Ionic liquid designed for PEDOT:PSS conductivity enhancement. *Journal of the American Chemical Society* **140**, 5375–5384 (2018).
41. De Izarra, A., Choi, C., Jang, Y. H. & Lansac, Y. Ionic Liquid for PEDOT:PSS Treatment. Ion Binding Free Energy in Water Revealing the Importance of Anion Hydrophobicity. *The Journal of Physical Chemistry B* **125**, 1916–1923 (2021).
42. Li, X. *et al.* Deciphering the superior thermoelectric property of post-treatment-free PEDOT:PSS/IL hybrid by X-ray and neutron scattering characterization. *npj Flexible Electronics* **6**, 6 (2022).
43. Han, M. *et al.* Insight into the Electrical Double Layer of Ionic Liquids Revealed through Its Temporal Evolution. *Advanced Materials Interfaces* **7**, 2001313 (2020).
44. Kong, M., Garriga, M., Reparaz, J. S. & Alonso, M. I. Advanced optical characterization of PEDOT:PSS by combining spectroscopic ellipsometry and Raman scattering. *ACS Omega* **7**, 39429–39436 (2022).
45. Jucius, D. *et al.* Structure and properties of dual-doped PEDOT:PSS multilayer films. *Materials Research* **22**, e20190134 (2019).
46. Kasha, M. Energy transfer mechanisms and the molecular exciton model for molecular aggregates. *Radiation Research* **20**, 55–70 (1963).
47. Hestand, N. J. & Spano, F. C. Expanded theory of H-and J-molecular aggregates: the effects of vibronic coupling and intermolecular charge transfer. *Chemical Reviews* **118**, 7069–7163 (2018).
48. Spano, F. C. Modeling disorder in polymer aggregates: The optical spectroscopy of regioregular poly (3-hexylthiophene) thin films. *The Journal of Chemical Physics* **122** (2005).
49. Kaake, L., Barbara, P. F. & Zhu, X.-Y. Intrinsic charge trapping in organic and polymeric semiconductors: a physical chemistry perspective. *The Journal of Physical Chemistry Letters* **1**, 628–635 (2010).
50. Clark, J., Chang, J.-F., Spano, F. C., Friend, R. H. & Silva, C. Determining exciton bandwidth and film microstructure in polythiophene films using linear absorption spectroscopy. *Applied Physics Letters* **94** (2009).
51. Parisi, G. Nobel lecture: Multiple equilibria. *Reviews of Modern Physics* **95**, 030501 (2023).
52. Dijk, G., Pas, J., Markovic, K., Scancar, J. & O'Connor, R. P. PEDOT:PSS-coated platinum electrodes for neural stimulation. *APL Bioengineering* **7**, 046117 (Dec. 2023).
53. Ilavsky, J. Nika: software for two-dimensional data reduction. *Journal of Applied Crystallography* **45**, 324–328 (2012).
54. Oosterhout, S. D. *et al.* Mixing behavior in small molecule: fullerene organic photovoltaics. *Chemistry of Materials* **29**, 3062–3069 (2017).

55. Frisch, M. J. *et al. Gaussian 16 Revision C.01* Gaussian Inc. Wallingford CT. 2016.
56. Becke, A. D. Density-functional exchange-energy approximation with correct asymptotic behavior. *Physical Review A* **38**, 3098 (1988).
57. Lee, C., Yang, W. & Parr, R. G. Development of the Colle-Salvetti correlation-energy formula into a functional of the electron density. *Physical Review B* **37**, 785 (1988).
58. Slater, J. C. *Quantum Theory of Molecules and Solids: The Self-Consistent Field for Molecules and Solids* (McGraw-Hill, New York, 1974).

Acknowledgments

L.M.B. acknowledges the German Academic Exchange Service (DAAD) and the Graduate Academy TU Dresden for support.

Author Contributions

L.M.B. and A.S. conceived the study. L.M.B. performed the electrical characterizations. T.J.Q. performed the XPS characterization. L.M.B. and G.L. carried out any optical spectroscopy. N.S. performed the DFT simulations. A.M. and C.C. carried out the GIWAXS measurement. G.D. fabricated the OECT devices. L.M.B. carried out the vibronic fitting and general data analysis. H.K. and K.L. provided guidance on data interpretation. L.M.B. wrote the manuscript, with input of G.L., T.J.Q., and G.D. All authors contributed to manuscript editing.

Additional Information

Additional information is given in the supplementary information.

Competing Financial Interests

The authors declare no competing interests.

Electron–Ion Coupling Breaks Energy Symmetry in Organic Electrochemical Transistors

Lukas M. Bongartz^{1,2*}, Garrett LeCroy¹, Tyler J. Quill¹, Nicholas Siemons¹, Gerwin Dijk¹, Adam Marks¹, Christina Cheng¹, Hans Kleemann², Karl Leo², Alberto Salleo¹

¹Department of Materials Science and Engineering, Stanford University, Stanford, CA 94305, USA

²Institute for Applied Physics, Technische Universität Dresden, Nöthnitzer Str. 61, 01187 Dresden, Germany

Supplementary Information

Contents

Supplementary Figures

Fig. S1	Molecular structure of PEDOT:PSS
Fig. S2	OECT transfer characteristics after [EMIM][EtSO ₄] post-treatment
Fig. S3	OECT transfer characteristics for different OMIECs and electrolytes
Fig. S4	Transfer curve recording with reference electrode
Fig. S5	XPS thin-film analysis (C 1s and S 2p core levels)
Fig. S6	GIWAXS diffraction pattern
Fig. S7	Thin-film UV-Vis spectroscopy
Fig. S8	Thin-film IR spectroscopy
Fig. S9	Raman spectroscopy
Fig. S10	Raman peak analysis
Fig. S11	Spectroelectrochemistry with [EMIM][EtSO ₄]
Fig. S12	Spectroelectrochemistry with [EMIM][TFSI]
Fig. S13	Spectroelectrochemistry with NaCl
Fig. S14	Vibronic transitions in spectroelectrochemistry
Fig. S15	De-/doping cycle of PEDOT:PSS and differential absorbance
Fig. S16	Mobility measurements
Fig. S17	XPS spectra (S 2p) of PEDOT:PSS for molar ratio estimation
Fig. S18	XPS spectra (O 1s) of PEDOT:PSS for ion exchange estimation

Supplementary Tables

Table S1	IR peak assignment
Table S2	Raman peak assignment
Table S3	PEDOT:PSS molar ratios estimated from XPS
Table S4	Ion exchange ratios estimated from XPS

Supplementary Notes

Supplementary Note 1: Mobility Measurements	
Supplementary Note 2: XPS Ratio Estimations	
Supplementary Note 3: Ion Exchange Estimations	
Supplementary Note 4: DFT Calculations	
Supplementary Note 5: Absorbance Fits for Spectroelectrochemistry	

Supplementary Figures

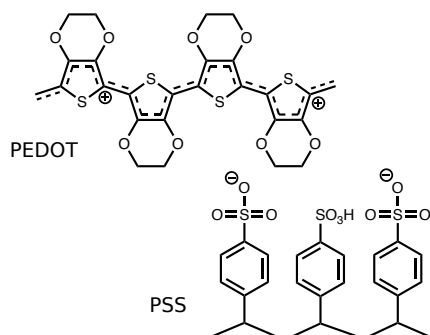


Fig. S1: Molecular structure of PEDOT:PSS. PEDOT:PSS is a blend of the electronic conductor poly(3,4-ethylenedioxythiophene) (PEDOT) doped with the polyanion and ionic conductor polystyrene sulfonate (PSS).

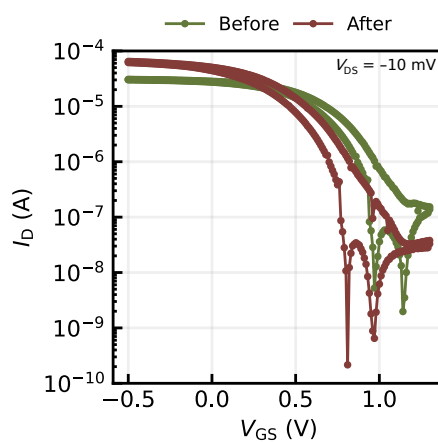


Fig. S2: OECT transfer characteristics after [EMIM][EtSO₄] post-treatment. An OECT was exposed to [EMIM][EtSO₄] for 5 min, rinsed with deionized water, and measured with 100 mM aqueous NaCl electrolyte (before and after exposure, respectively). The treatment reduces the threshold voltage, raises the on-current, and lowers the off-current.

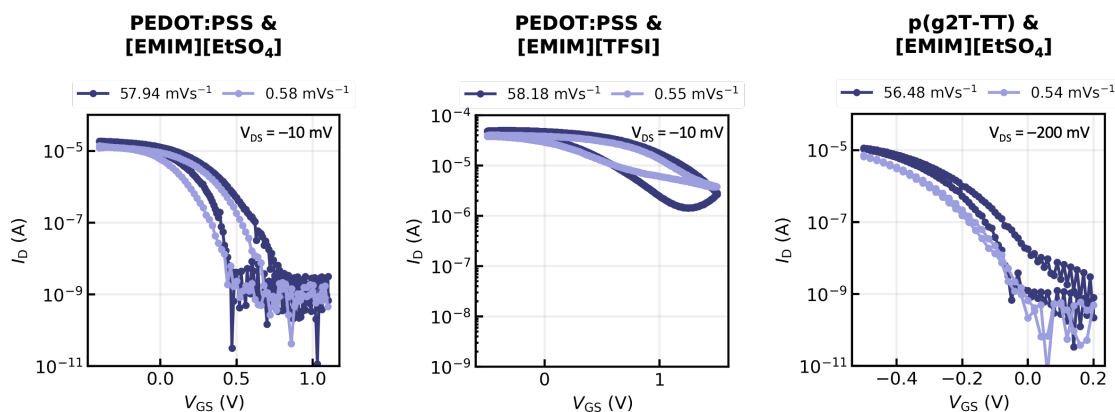


Fig. S3: OECT transfer characteristics for different OMIECs and electrolytes. Transfer characteristics at different scan rates for OECTs based on PEDOT:PSS with [EMIM][EtSO₄] and [EMIM][TFSI] electrolyte, as well as for an OECT with [EMIM][EtSO₄] electrolyte and a poly(2-(3,3'-bis(2-(2-(2-methoxyethoxy)ethoxy)ethoxy)-[2,2'-bithiophen]-5-yl) thieno [3,2-b]thiophene) (p(g2T-TT)) channel and gate.

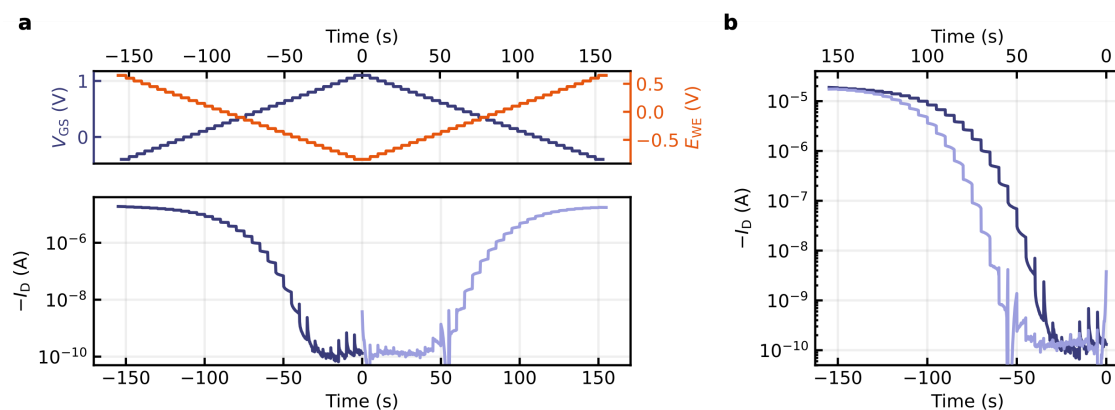


Fig. S4: Transfer curve recording with reference electrode. The OECT is operated while using an Ag quasi-reference electrode immersed in the electrolyte ($V_{DS} = -10$ mV). (a) The measured potential E_{WE} shifts symmetrically to the applied voltage V_{GS} , while the drain current I_D follows as expected. (b) I_D -response folded around the axis at 0 s.

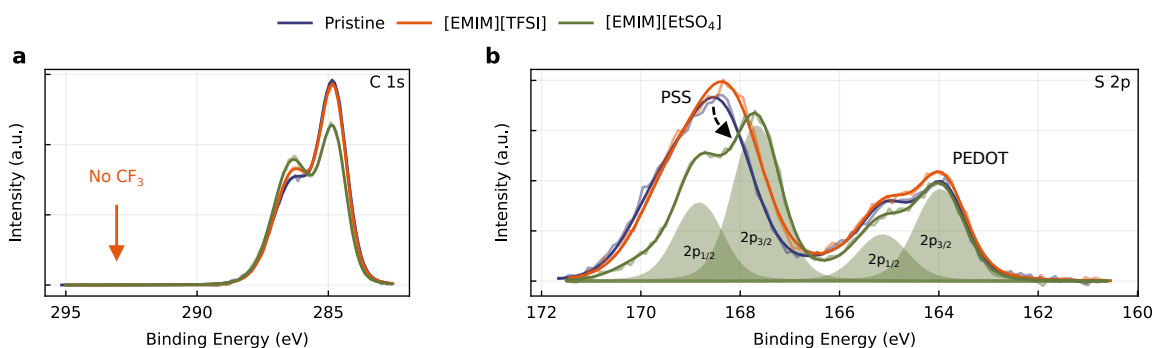


Fig. S5: XPS thin-film analysis (C 1s and S 2p core levels). XPS spectra of PEDOT:PSS thin-films exposed to [EMIM][TFSI] and [EMIM][EtSO₄]. (a) C 1s core level region. No CF₃ signal is detected for the [EMIM][TFSI]-treated sample (CF₃ ~ 293 eV⁻¹). [EMIM][EtSO₄] induces an altered ratio of C–O and C–C signal (C–C decreases). (b) S 2p core level region. [EMIM][TFSI] does not cause a significant change to the ratio of PEDOT to PSS, aligning with the minute decrease observed in the O 1s data (Fig. 2c). With [EMIM][EtSO₄], on the other hand, the fraction of PEDOT is increased, driven by a removal of PSS. Here, the PSS signal also undergoes a marked shift to lower binding energy. This shift is on the one hand attributed to an overlap with the signal of retained [EtSO₄]⁻, having a slightly decreased binding energy compared to the SO₃-group of PSS². Moreover, it underlines the binding of the two anionic species to [EMIM]⁺, the π -system of which strongly increases the vicinal electron density around the sulfur atoms.

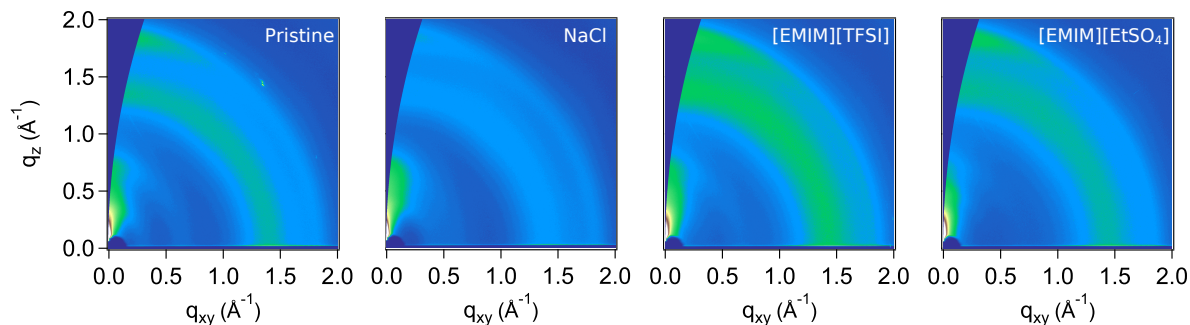


Fig. S6: GIWAXS diffraction pattern. GIWAXS is performed for thin-films of pristine PEDOT:PSS and after exposure to NaCl (100 mM), [EMIM][TFSI], and [EMIM][EtSO₄].

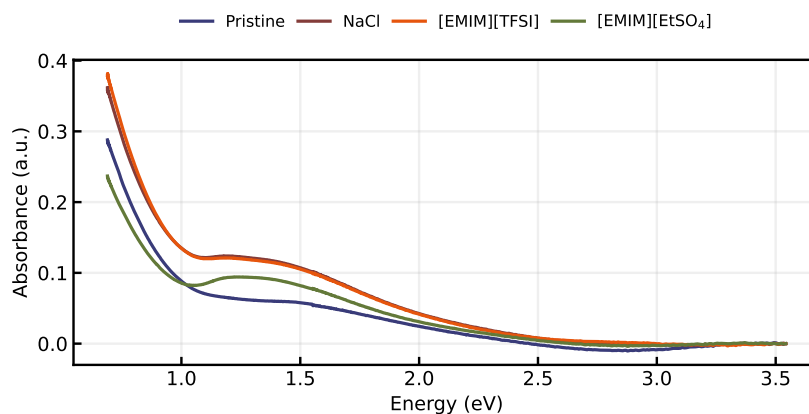


Fig. S7: Thin-film UV-Vis spectroscopy. PEDOT:PSS thin-films were temporarily exposed to the electrolytes and analyzed by UV-Vis spectroscopy. No significant changes to the absorbance are found, except a seemingly more distinct polaron absorbance at around 1.3 eV for the sample treated with [EMIM][EtSO₄].

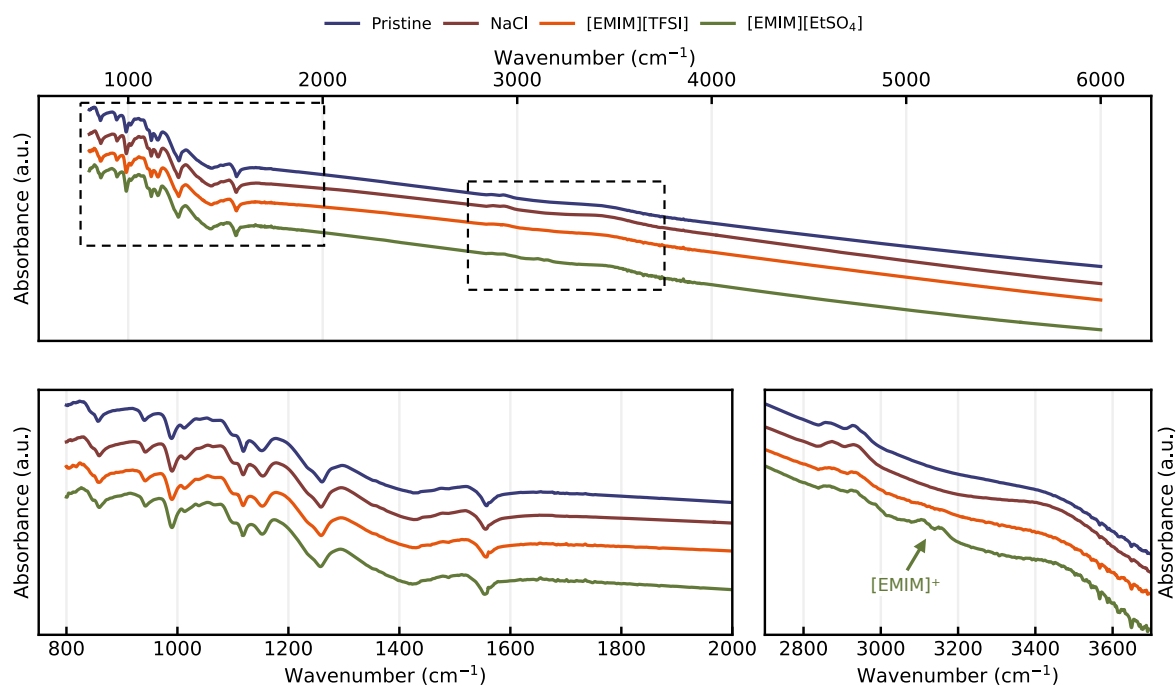


Fig. S8: Thin-film IR spectroscopy. IR spectra are recorded for thin-films of pristine and electrolyte-treated PEDOT:PSS. No significant changes are found, except for an additional feature around 3110–3160 cm⁻¹ for the sample treated with [EMIM][EtSO₄]. The signal can be assigned to the [EMIM]⁺ cation retained in the film³. Further peak assignment is provided in Tab. S1.

Table S1: IR peak assignment.

Wavenumber (cm ⁻¹)	Lit. (cm ⁻¹)	Mode	Ref.
857, 940	842, 955	C-S-C	5
989, 1119	1055, 1126	C-O-C	5
1013	1026	C-S (PSS)	5
1153	1172	S=O (sym.)	5
1261	1273	C-C, S=O (asym.)	5
1429	1412–1418	C=C (sym.)	5
1557	1540–1550	C=C (asym.)	5
2866, 2932	2851, 2925	C-H	4
~ 3440	~ 3450	O-H	4
3110, 3155	3103, 3151	C-H ([EMIM])	3

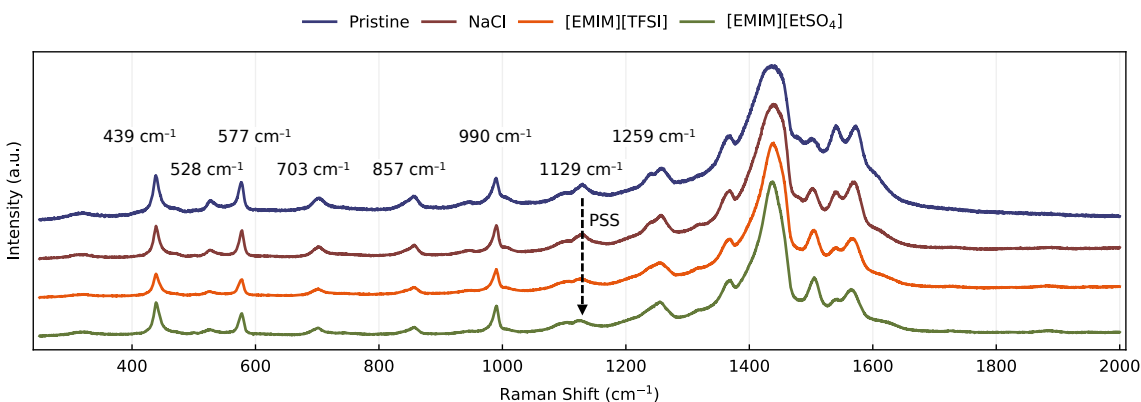
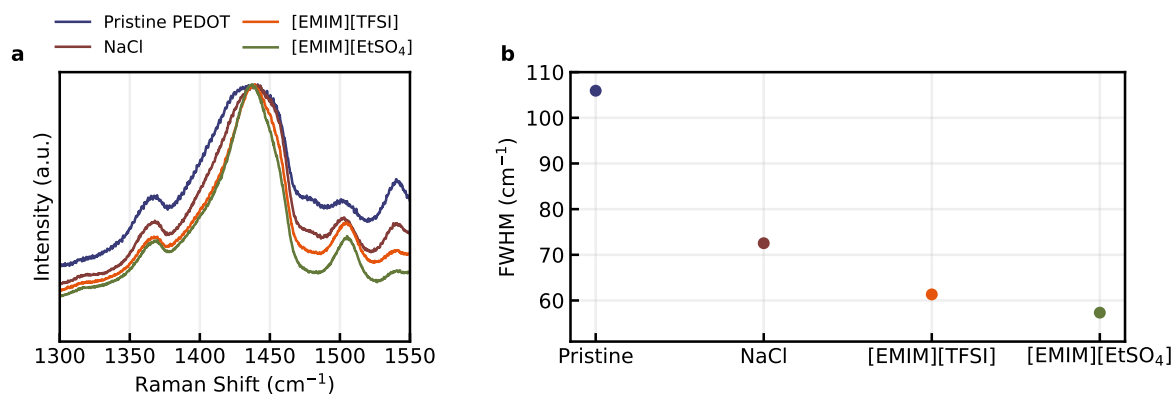
**Fig. S9: Raman spectroscopy.** Raman spectra recorded with $\lambda_{\text{exc}} = 532$ nm. A comprehensive peak assignment is provided in Tab. S2. The high-energy range is shown isolated in Fig. 3c.**Fig. S10: Raman peak analysis.** (a) Principle Raman peaks are identified at 1441 cm⁻¹ (pristine), 1439 cm⁻¹ (NaCl), 1439 cm⁻¹ ([EMIM][TFSI]), and 1438 cm⁻¹ ([EMIM][EtSO₄]). (b) Electrolyte exposure effects a reduction in bandwidth of the principle peak, evident in a decreasing full width at half maximum (FWHM). For [EMIM][EtSO₄], the reduction equates to approximately 45%.

Table S2: Raman peak assignment. Literature values correspond to the same excitation wavelength ($\lambda_{\text{exc}} = 532 \text{ nm}$).

Raman Shift (cm^{-1})	Lit. ⁶ (cm^{-1})	Mode
439	439	
528	~ 525	
577	577	Oxyethylene ring deform.-vibr.
703	702	C-S-C (sym.) deform.
857	855	Oxyethylene ring deform.-vibr. (C-H bending)
990	988	Oxyethylene ring deform.-vibr.
1129	1124	PSS
1259	1256	$C_{\alpha}-C_{\alpha'}$ inter-ring stretch.-vibr.
1367	1367	$C_{\beta}-C_{\beta}$ stretch.-deform.
1438	1428	$C_{\alpha}=C_{\beta}$ (sym.) stretch.-vibr.
1502	1486	$C_{\alpha}=C_{\beta}$ (asym.) stretch.-vibr. (mid-chain)
1540	1537	$C_{\alpha}=C_{\beta}$ (asym.) stretch.-vibr. (split)
1572	1569	$C_{\alpha}=C_{\beta}$ (asym.) stretch.-vibr. (end-chain)

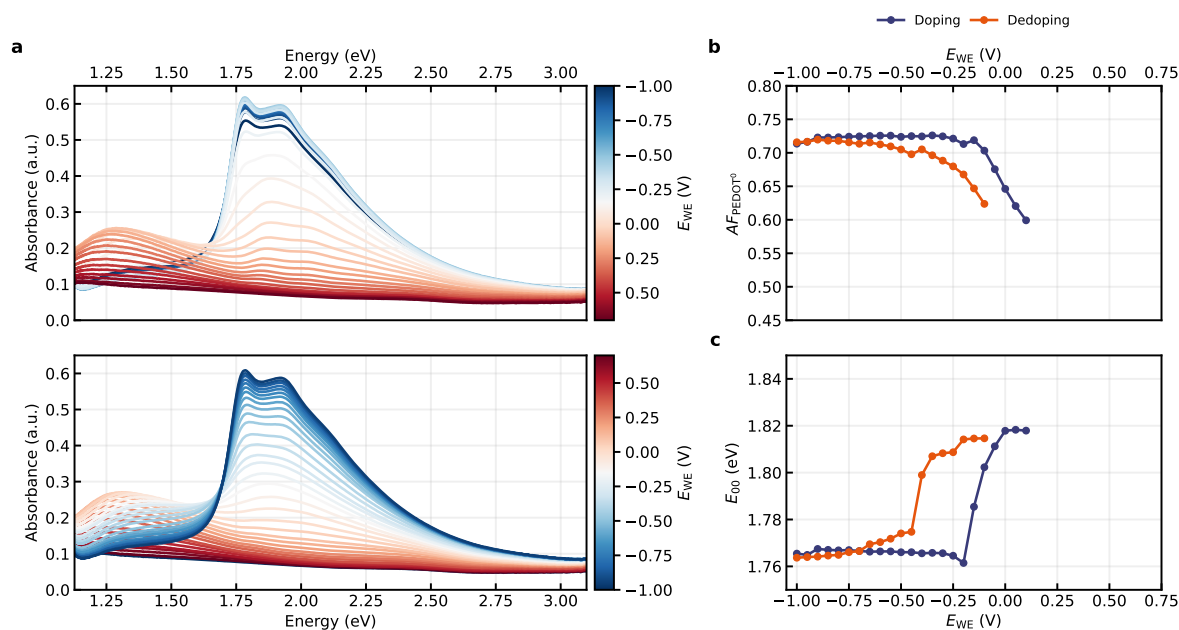


Fig. S11: Spectroelectrochemistry with [EMIM][EtSO₄]. (a) Absorbance spectra recorded under doping and dedoping. (b) Aggregate fraction and (c) E_{00} energies under doping and dedoping. The exceeding intensity of the 0-0 transition compared to the 0-1 transition indicates a dominance of intrachain coupling.

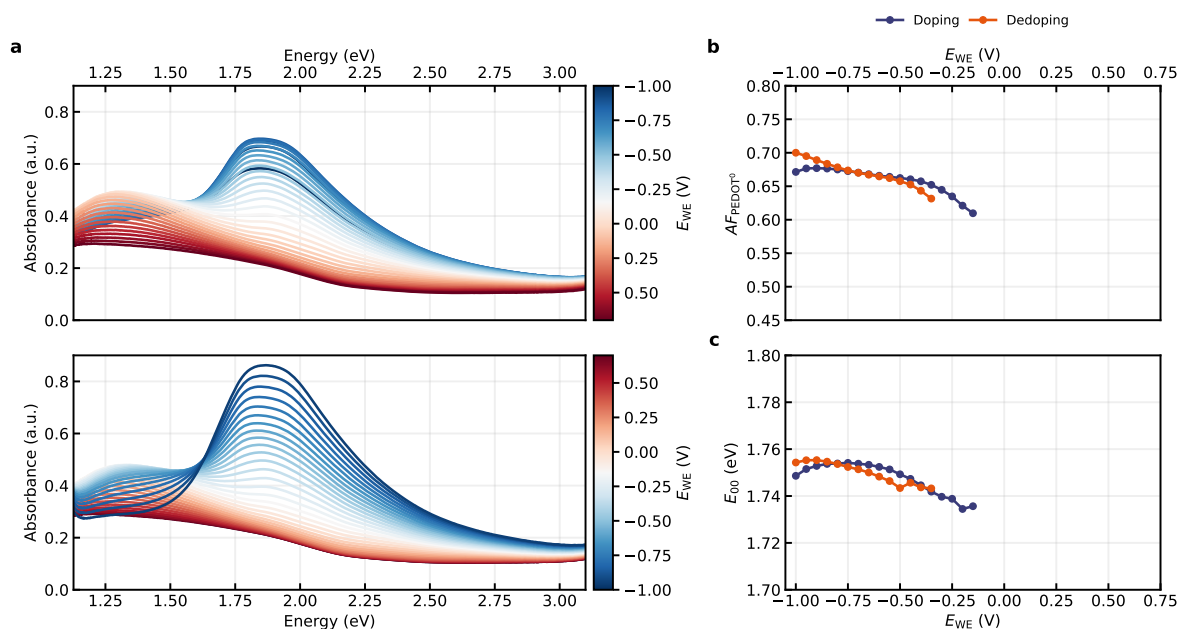


Fig. S12: Spectroelectrochemistry with [EMIM][TFSI]. (a) Absorbance spectra recorded under doping and dedoping. (b) Aggregate fraction and (c) E_{00} energies under doping and dedoping.

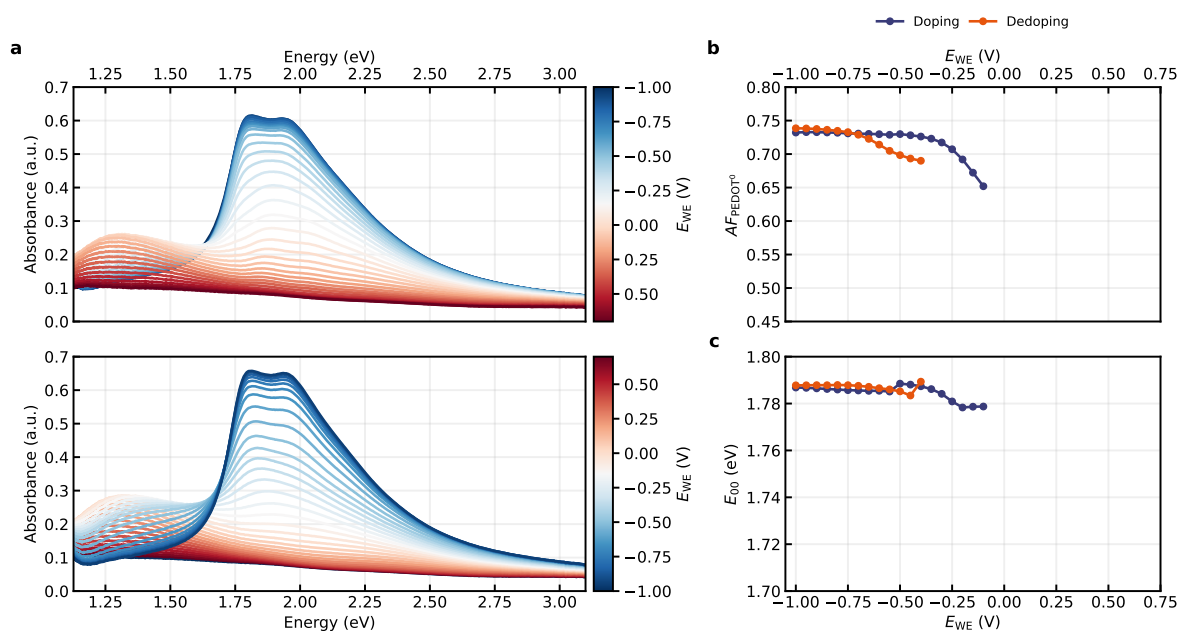


Fig. S13: Spectroelectrochemistry with NaCl (100 mM). (a) Absorbance spectra recorded under doping and dedoping. (b) Aggregate fraction and (c) E_{00} energies under doping and dedoping. The balancing intensity of the 0-0 transition compared to the 0-1 transition indicates a balance of intra- and interchain coupling.

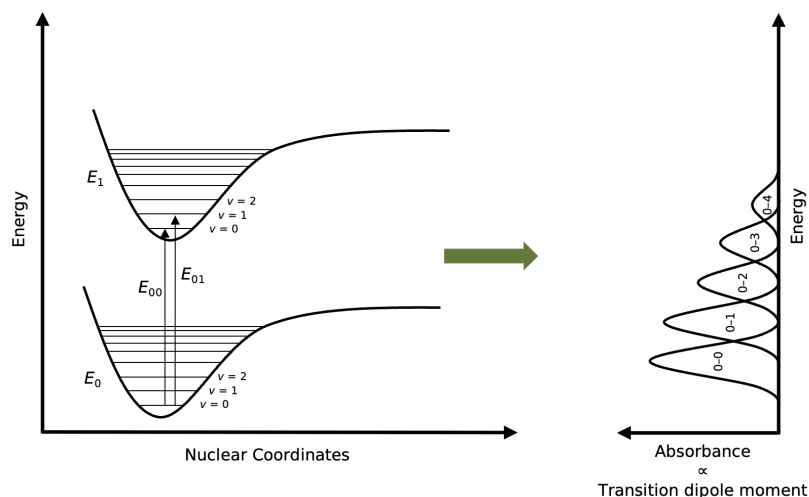


Fig. S14: Vibronic transitions. Schematic illustration of the electronic and vibrational transitions underlying the absorbance spectra in spectroelectrochemistry. Electronic excitations go along with subordinate vibrational transitions. The energetic difference between the ground (E_0) and excited (E_1) state can be traced by the absorbance line E_{00} , with smaller values (red-shift) indicating a thermodynamically stabilized species.

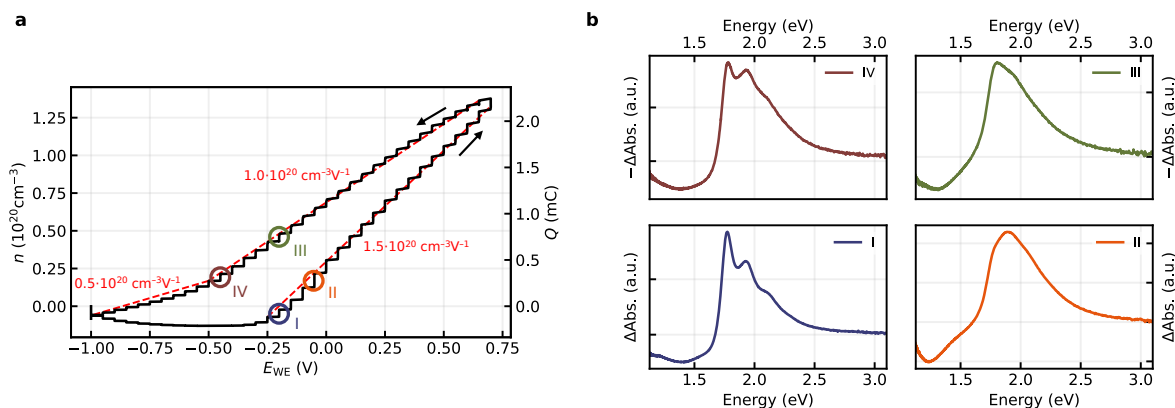


Fig. S15: De-/doping cycle of PEDOT:PSS and differential absorbance. (a) Charge carrier density n as a function of applied potential E_{WE} (V vs. Ag/AgCl). Different charging efficiencies (differential capacitances) are found for charging and discharging. The latter shows a flattening kink at around $E_{WE} = -0.5$ V, indicating energetic impediment. (b) Differential absorbance spectra corresponding to the four potential steps highlighted in (a). Ordered species are charged first, followed by disordered, more amorphous entities. Discharging the former is offset to more negative potentials, indicating an energetic stabilization of the doped state. Note also the difference in relative peak intensities between I (doping) and IV (dedoping), indicative of a disruption of the local electronic environment.

Supplementary Notes

Supplementary Note 1: Mobility Measurements

We study the hole mobility in OECTs with the [EMIM][EtSO₄] electrolyte using a previously reported pulsed current technique^{7,8}. We perform measurements before and after biasing the device at $V_{GS} = 1$ V for 60 s to probe the doped and undoped state of the channel.

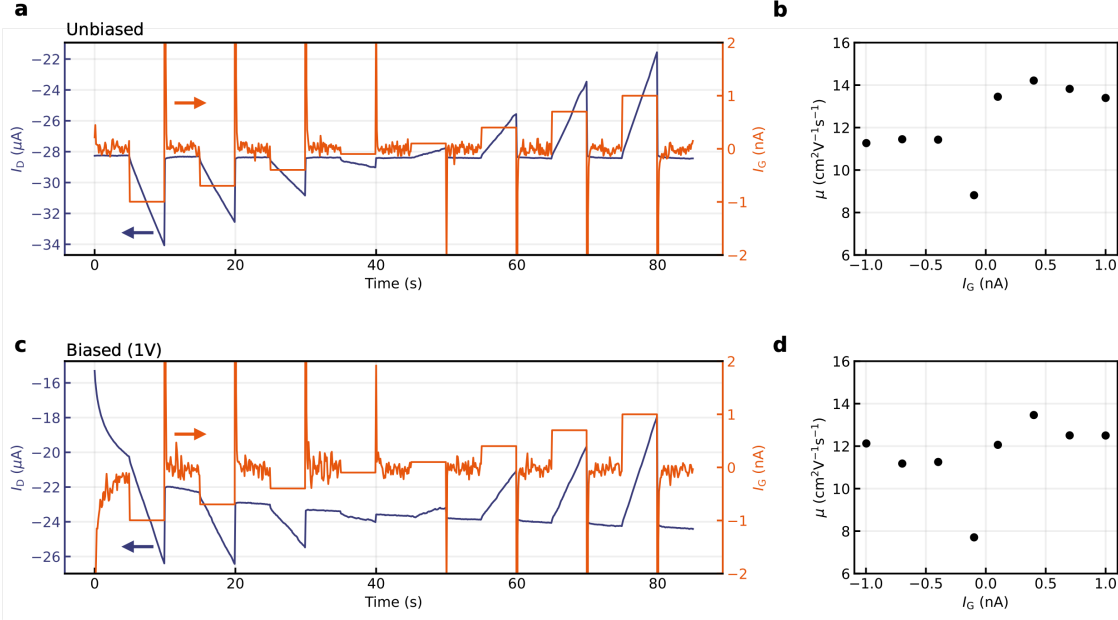


Fig. S16: Mobility measurements. Hole mobilities are measured for an OECT with PEDOT:PSS channel and [EMIM][EtSO₄] electrolyte by a previously reported pulsed current technique^{7,8}. (a, b) Before biasing and (c, d) after biasing the OECT at $V_{GS} = 1$ V for 60 s to measure the doped and undoped state.

The drain current I_D is recorded for gate current pulses I_G . From this, the mobility follows as

$$\mu = \frac{\partial I_D}{\partial t} \cdot \frac{L^2}{V_{DS} \cdot I_G} \quad (\text{S1})$$

for the individual current pulse, where $L = 100$ μm and $V_{DS} = -0.01$ V. 8 pulses of increasing I_G are applied for 5 s each, yielding mobilities as shown in Fig. S16b and d, representing the doped and undoped state of the channel. The averaged mobilities result as

$$\begin{aligned} \mu_d &= (12.2 \pm 0.6) \text{ cm}^2 \text{ V}^{-1} \text{ s}^{-1} \quad \text{and} \\ \mu_u &= (11.6 \pm 0.6) \text{ cm}^2 \text{ V}^{-1} \text{ s}^{-1}, \end{aligned}$$

with uncertainties corresponding to the standard error of the mean.

Supplementary Note 2: XPS Ratio Estimations

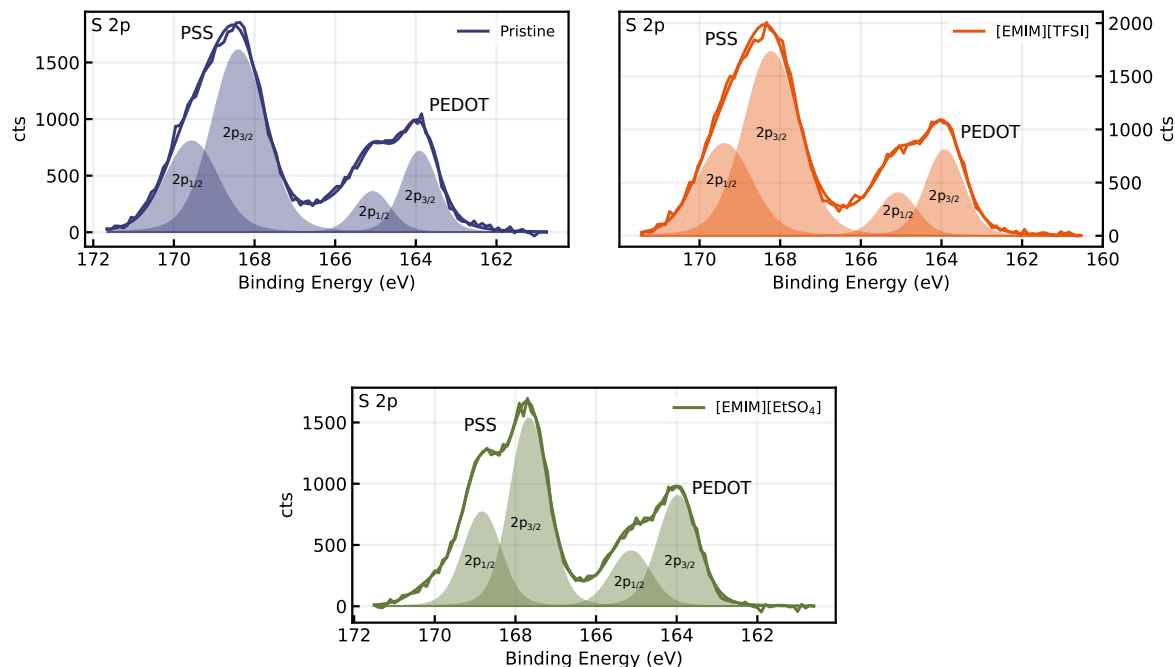


Fig. S17: XPS spectra (S 2p) of PEDOT:PSS for molar ratio estimation. XPS (S 2p) spectra and fits of pristine PEDOT:PSS and after exposure to [EMIM][TFSI] and [EMIM][EtSO₄]. The integrated fits serve to estimate the ratio of PEDOT to PSS.

We calculate PEDOT-to-PSS (molar) ratios from the XPS data, respectively the fits of the same (Fig. S17). For this, spectra are background-subtracted using a Shirley-type background and smoothed by means of a Savitzky-Golay filter. Peaks are fitted with Gaussian-Lorentzian lineshapes. PEDOT:PSS ratios are inferred from the integrated 2p_{1/2} and 2p_{3/2} signals of PEDOT and PSS, where we assume similar cross-sections for photoelectron emission and therefore similar sensitivities:

$$cts^{S^{2p}}(\text{PEDOT}) = \int S_{2p_{2p_{1/2}}}(\text{PEDOT})dE + \int S_{2p_{2p_{3/2}}}(\text{PEDOT})dE \quad (\text{S2})$$

$$cts^{S^{2p}}(\text{PSS}) = \int S_{2p_{2p_{1/2}}}(\text{PSS})dE + \int S_{2p_{2p_{3/2}}}(\text{PSS})dE \quad (\text{S3})$$

Table S3: PEDOT:PSS molar ratios estimated from XPS.

System	$cts^{S^{2p}}(\text{PEDOT})$	$cts^{S^{2p}}(\text{PSS})$	R_M (PEDOT:PSS)
Pristine	1217.35	4125.70	3.39
[EMIM][TFSI]	1471.60	4563.76	3.10
[EMIM][EtSO ₄]	1737.54	2803.69	1.61

Our calculations show that [EMIM][EtSO₄] considerably reduces the relative amount of PSS compared to the pristine sample. This process goes along with an ion exchange, where residual

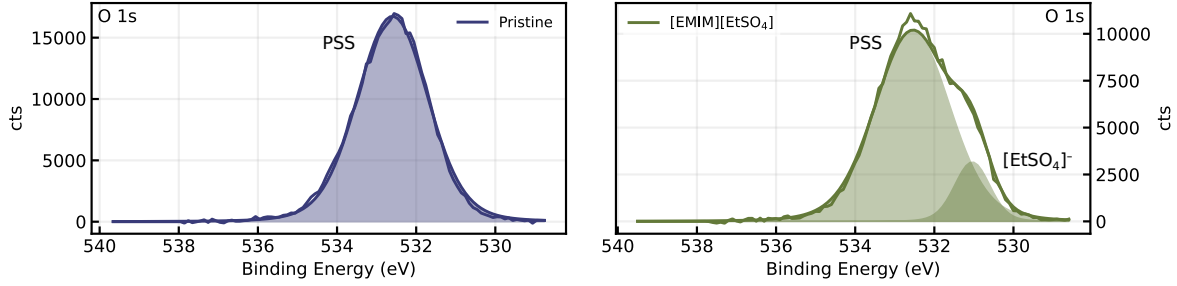


Fig. S18: XPS spectra (O 1s) of PEDOT:PSS for ion exchange estimation. XPS (O 1s) spectra and fits of pristine PEDOT:PSS and after exposure to [EMIM][EtSO₄].

Na⁺ is replaced by [EMIM]⁺ in addition to [EMIM][EtSO₄] being retained, giving rise to the composition illustrated in Fig. 2d and aligning with reports by Kee et al.⁹.

We further estimate the degree of ion exchange from the XPS data and in particular, from the O 1s core level region (Fig. S18). The signal of the pristine sample can be attributed solely to PSS, while the [EMIM][EtSO₄]-treated sample shows signals for both PSS and [EtSO₄]⁻. To relate the data sets to the same basis (PEDOT), we use the molar ratios of Tab. S3 and calculate the ratio of ion exchange as follows:

$$R_{\text{IE}} = R_{\text{M}} \cdot \frac{\int \text{O } 1\text{s}([\text{EtSO}_4]^-)dE}{\int \text{O } 1\text{s}(\text{PSS})dE} = R_{\text{M}} \cdot \frac{\text{cts}^{\text{O } 1\text{s}}([\text{EtSO}_4]^-)}{\text{cts}^{\text{O } 1\text{s}}(\text{PSS})} \quad (\text{S4})$$

Table S4: Ion exchange ratios estimated from XPS.

System	cts ^{O 1s} (PSS)	cts ^{O 1s} ([EtSO ₄] ⁻)	R _M	R _{IE}
Pristine	38907.29		3.39	
[EMIM][EtSO ₄]	25046.53	3694.77	1.61	0.24

We calculate the ion exchange ratio as approximately 24%. This figure does not deviate significantly from the estimate in Supplementary Note 3, where a theoretical exchange ratio of 31.7% is derived from DFT literature data.

Since we infer the ion exchange ratio by relating information from the S 2p core level region to the O 1s region, we verify this approach by comparing the ratio of PEDOT-equivalents for the pristine and [EMIM][EtSO₄]-treated sample in the O 1s and S 2p spectra:

$$\frac{\text{cts}_{\text{Pristine}}^{\text{O } 1\text{s}}(\text{PSS})}{\text{cts}_{[\text{EMIM}][\text{EtSO}_4]}^{\text{O } 1\text{s}}(\text{PSS})} \cdot \frac{R_{\text{M}}^{[\text{EMIM}][\text{EtSO}_4]}}{R_{\text{M}}^{\text{Pristine}}} = 0.74 \quad (\text{S5})$$

$$\frac{\text{cts}_{\text{Pristine}}^{\text{S } 2\text{p}}(\text{PEDOT})}{\text{cts}_{[\text{EMIM}][\text{EtSO}_4]}^{\text{S } 2\text{p}}(\text{PEDOT})} = 0.70 \quad (\text{S6})$$

The deviation between the two ratios is only around 6%, which we consider small enough to motivate our previous calculations.

Supplementary Note 3: Ion Exchange Estimations

Using DFT, de Izarra et al. calculated the ion exchange free energy for PEDOT:PSS and [EMIM][EtSO₄] as 1.9 kJ mol⁻¹, equivalent to 19.7 meV¹⁰. Given a Boltzmann distribution, the exchange ratio follows as

$$\frac{N_2}{N_1} = e^{-\frac{\Delta G}{k_B T}}, \quad (\text{S7})$$

which suggests that at room temperature (298.15 K), approximately 31.7% of the entities are in the ion-transferred state.

Supplementary Note 4: DFT Calculations

To understand the impact of intra-chain structure on the measured Raman spectra, PEDOT oligomers consisting of 10 repeat units and three holes were studied using density functional theory (DFT). Using oligomers of ten repeat units allowed for appropriate delocalization of excess charges and charge densities for doped PEDOT¹¹, while also allowing for structures of representative sizes^{12,13} to be simulated. All simulations were performed using doublet multiplicity.

Simulations were performed using two distinct initial configurations of PEDOT. The first with all inter-thiophene dihedrals set to zero, and the second with the central inter-thiophene dihedral set to 140°. These two structures were geometry relaxed using DFT with a B3LYP¹⁴⁻¹⁶ functional and 6-311G basis set. Following the geometry relaxation, a frequency analysis was performed to obtain their vibrational frequencies corresponding Raman activities, allowing for the dependency on the frequency of the incident Raman laser. An incident laser energy of 2.329 eV was used, matching that of the experiments. DFT calculations were carried out using the Gaussian16 software package¹⁷.

The Raman spectra were obtained by fitting Lorentzian functions to the Raman frequencies, each with a maximum corresponding to the Raman activity and a full-width-half-maximum of 5 cm⁻¹.

Supplementary Note 5: Absorbance Fits for Spectroelectrochemistry

Absorbance (Abs.) in this work refers to

$$\text{Abs.} = -\log\left(\frac{I}{I_0}\right), \quad (\text{S8})$$

where I and I_0 are the intensities of light transmitted through sample and reference. Eq. S8 directly relates to the oscillator strength of a transition by the Beer-Lambert law. We fit the optical absorbance spectra to the vibronic model developed by Spano¹⁸, using methods previously shown applicable for other thiophene-based polymers¹⁹. The model takes a Holstein Hamiltonian as a basis and assumes a molecular crystal with electron-phonon coupling by a single phonon mode. Absorbance results as a function of energy (frequency ω) by

$$A(\omega) = C \sum_{m=0} \frac{e^{-\lambda^2} \lambda^{2m}}{m!} \left(1 - \frac{W e^{-\lambda^2}}{2E_p} G(\lambda^2; m)\right)^2 \Gamma\left(\hbar\omega - E_{00} - mE_p - 0.5W\lambda^{2m}e^{-\lambda^2}\right) \quad (\text{S9})$$

with

$$G(\lambda^2; m) = \sum_{\substack{n=0,1,\dots \\ n \neq m}} \frac{\lambda^{2n}}{n!(n-m)} \quad \text{and} \quad (\text{S10})$$

$$\Gamma(X) = \frac{1}{\sigma\sqrt{2\pi}} e^{-\frac{X^2}{2\sigma^2}}, \quad (\text{S11})$$

where \hbar is the reduced Planck constant. Fits are performed with four free parameters, being the scaling factor C , the exciton bandwidth W , the 0–0 vibronic transition energy E_{00} , and the peak linewidth σ . For W , $W = 4J_{\text{inter}}$ applies, with J_{inter} denoting interchain exciton coupling. λ^2 is the Huang-Rhys factor, essentially denoting the strength of electron-phonon coupling. It is taken here as $\lambda^2 = 0.95$, based on previous works on thiophene-based polymers^{19,20}. E_p is a vibrational energy combining multiple phonon modes stemming from the thiophene backbone and was kept at $E_p = 0.166$ V in this work. We consider the energetically five lowest vibronic transitions (0–0 to 0–4), thus taking the absorbance sum from $m = 0$ to $m = 4$. Fits were performed by a Levenberg-Marquardt algorithm with the modifications introduced by Fletcher²¹.

The aggregate fraction (AF) is calculated from the integrated spectral intensities as estimated from fitting Eq.S9. These are assigned to aggregate absorbance A_{Agg} , while the remainder to the total experimental absorbance is assigned to amorphous regions A_{Amor} . AF results as the ratio of integrated aggregate absorbance to the integrated absorbance of both aggregates and amorphous regions, weighted by the molar extinction coefficients ϵ_{Agg} and ϵ_{Amor} :

$$AF = \frac{\epsilon_{\text{Agg}} \int A_{\text{Agg}}(E) dE}{\epsilon_{\text{Agg}} \int A_{\text{Agg}}(E) dE + \epsilon_{\text{Amor}} \int A_{\text{Amor}}(E) dE} \quad (\text{S12})$$

Integrals are taken in a range of ~ 1.13 – 3.10 eV (400–1100 nm), corresponding to our setup's detector limits. ϵ_{Agg} and ϵ_{Amor} are adopted from values reported on poly(3-hexylthiophen-2,5-diyl) (P3HT) with $\epsilon_{\text{Agg}} = 1.39\epsilon_{\text{Amor}}$ ²².

Supplementary References

1. Foelske-Schmitz, A, Weingarh, D & Kötz, R. XPS analysis of activated carbon supported ionic liquids: Enhanced purity and reduced charging. *Surface Science* **605**, 1979–1985 (2011).
2. Jurado, L. A. *et al.* Effect of the environmental humidity on the bulk, interfacial and nanoconfined properties of an ionic liquid. *Physical Chemistry Chemical Physics* **18**, 22719–22730 (2016).
3. Wheeler, J. L., Pugh, M., Atkins, S. J. & Porter, J. M. Thermal breakdown kinetics of 1-ethyl-3-methylimidazolium ethylsulfate measured using quantitative infrared spectroscopy. *Applied Spectroscopy* **71**, 2626–2631 (2017).
4. Karri, S. N. & Srinivasan, P. Synthesis of PEDOT:PSS using benzoyl peroxide as an alternative oxidizing agent for ESD coating and electro-active material in supercapacitor. *Materials Science for Energy Technologies* **2**, 208–215 (2019).
5. Petsagkourakis, I. *et al.* Improved Performance of Organic Thermoelectric Generators Through Interfacial Energetics. *Advanced science* **10**, 2206954 (2023).
6. Jucius, D. *et al.* Structure and properties of dual-doped PEDOT:PSS multilayer films. *Materials Research* **22**, e20190134 (2019).
7. Bernardis, D. A. & Malliaras, G. G. Steady-state and transient behavior of organic electrochemical transistors. *Advanced Functional Materials* **17**, 3538–3544 (2007).
8. Keene, S. T. *et al.* Efficient electronic tunneling governs transport in conducting polymer-insulator blends. *Journal of the American Chemical Society* **144**, 10368–10376 (2022).
9. Kee, S. *et al.* Controlling molecular ordering in aqueous conducting polymers using ionic liquids. *Advanced Materials* **28**, 8625–8631 (2016).
10. De Izarra, A., Park, S., Lee, J., Lansac, Y. & Jang, Y. H. Ionic liquid designed for PEDOT:PSS conductivity enhancement. *Journal of the American Chemical Society* **140**, 5375–5384 (2018).
11. Kahol, P. *et al.* On metallic characteristics in some conducting polymers. *Synthetic Metals* **151**, 65–72 (2005).
12. Kim, D., Franco-Gonzalez, J. F. & Zozoulenko, I. How long are polymer chains in poly (3, 4-ethylenedioxythiophene): Tosylate Films? An insight from molecular dynamics simulations. *The Journal of Physical Chemistry B* **125**, 10324–10334 (2021).
13. Jain, K., Mehandzhiyski, A. Y., Zozoulenko, I. & Wågberg, L. PEDOT:PSS nanoparticles in aqueous media: A comparative experimental and molecular dynamics study of particle size, morphology and z-potential. *Journal of Colloid and Interface Science* **584**, 57–66 (2021).
14. Becke, A. D. Density-functional exchange-energy approximation with correct asymptotic behavior. *Physical Review A* **38**, 3098 (1988).
15. Lee, C., Yang, W. & Parr, R. G. Development of the Colle-Salvetti correlation-energy formula into a functional of the electron density. *Physical Review B* **37**, 785 (1988).
16. Slater, J. C. *Quantum Theory of Molecules and Solids: The Self-Consistent Field for Molecules and Solids* (McGraw-Hill, New York, 1974).
17. Frisch, M. J. *et al.* *Gaussian 16 Revision C.01* Gaussian Inc. Wallingford CT. 2016.

18. Spano, F. C. Modeling disorder in polymer aggregates: The optical spectroscopy of regioregular poly (3-hexylthiophene) thin films. *The Journal of Chemical Physics* **122** (2005).
19. LeCroy, G. *et al.* Role of aggregates and microstructure of mixed-ionic–electronic-conductors on charge transport in electrochemical transistors. *Materials Horizons* **10**, 2568–2578 (2023).
20. Clark, J., Silva, C., Friend, R. H. & Spano, F. C. Role of intermolecular coupling in the photophysics of disordered organic semiconductors: aggregate emission in regioregular polythiophene. *Physical Review Letters* **98**, 206406 (2007).
21. Fletcher, R. A modified Marquardt subroutine for non-linear least squares (1971).
22. Clark, J., Chang, J.-F., Spano, F. C., Friend, R. H. & Silva, C. Determining exciton bandwidth and film microstructure in polythiophene films using linear absorption spectroscopy. *Applied Physics Letters* **94** (2009).